



Project Number: 774571
Start Date of Project: 2017/11/01
Duration: 48 months



Type of document 4.5 – V1.0

Pest and disease detection

Dissemination level	PU
Submission Date	2020-06-08
Work Package	WP4
Task	T4:5
Type	Report
Version	1.0
Author	Steve Ahlswede, Sebastian Lamprecht, Rebecca Retzlaff,
Approved by	Andrea Gasparri + PMC

Executive Summary

This document comprises a detailed description of *Task 4.5 – Pest and Disease Detection* to identify pests and diseases using remote sensing data. The methods, findings and pest and disease severity maps presented in the given document serve as an input for *Task 5.4 – Major diseases Monitoring and Control* as well as a reference for *Task 4.6 – Water Stress Measurement*.

Furthermore, this document describes the monitoring concept and experimental setup to receive the required data quality for the PANTHEON project. The following sub-tasks have been addressed:

1. Elaboration of an experimental setup
2. UAV image pre-processing (based on *D4.3 – Aerial Image Processing Pipeline*)
3. UGV image pre-processing (based on *D4.1 – Multispectral LiDAR Point Clouds*)
4. Identification of sensitive spectral indices
5. Generation of disease severity maps

Table of Contents

Table of Contents.....	3
1 Introduction.....	7
1.1 Deviation from the task description	8
1.2 Relevant Pests and Diseases	8
2 Experimental setup.....	9
2.1 Trials.....	9
2.2 Ground Truth	11
2.2.1 Pests.....	11
2.2.2 Diseases	12
3 Field data	15
3.1 UAV Campaigns.....	15
3.2 UGV Campaigns	17
3.3 IoT data	17
4 Methods.....	18
4.1 Vegetation indices	18
4.2 UAV image pre-processing.....	19
4.2.1 Tetracam MCAW	19
4.2.2 Sony α 5100	20
4.2.3 Teax Thermal Camera	20
4.2.4 Orthomosaic generation	20
4.3 UGV image processing	21
4.4 Feature extraction.....	22
4.5 Identification of sensitive indices.....	23
5 Results and Discussion	24
5.1 UAV processing	24
5.1.1 Empirical line correction	24
5.1.2 Orthomosaics	26
5.2 Sensitivity of spectral indices	34
5.2.1 Pigments	34
5.2.2 Pests.....	34
5.2.3 Leaf anthracnosis	36
5.2.4 Bacterial spot necrosis	39
5.2.5 Nut necrosis	39
5.2.6 General Discussion	40
6 Conclusions	41
6.1 Completed tasks.....	41
6.2 Future Research	42
6.3 Criticalities and Mitigation Actions	42
6.4 Ongoing activities.....	43
7 References	44
8 Appendix Image Data.....	47

List of Figures

Fig. 1. Overview of the experimental setup of PANTHEON. 10

Fig. 2. Detail view of the trees assigned to the pest and disease trials. 10

Fig. 3. Branch with Styrofoam sphere and cage (background) and branch of interest marked with sphere (foreground). 11

Fig. 4. Boxplots of the ratio of damaged nuts per treatment group (left) and per tree (right). The whiskers extend to the data extremes. 12

Fig. 5. Necrotic leaf area associated with *Anthracosis* monitored in PANTHEON test site..... 13

Fig. 6. Development of *Nut Necrosis* on the fruits of the trees over time. 14

Fig. 7. Development of *Bacterial Spot Necrosis* on the tree canopy over time. 14

Fig. 8. Solar radiation during the UAV campaigns of 2019/06/02, 2019/07/14, 2019/07/21 and 2019/08/10 measured by the weather station of the field. 17

Fig. 9. Environmental conditions during the relevant time period recorded by the IoT network at the study site. 18

Fig. 10. Single band image from MicaSense RedEdge-M camera (left) and the mask used to determine the target branch pixels (right). 23

Fig. 11. Results of the empirical line calibration for Tetracam MCAW-6, flight *camp_2019-07-21_09-29-00*. 25

Fig. 12. Noisy band at 530nm for Tetracam MCAW-6 showing the reference panels. 26

Fig. 13. Orthomosaics from 21 July, 2019 (top-left: Sony RGB, top-right: McaW R900nm, G680nm, B550nm, bottom-center: Teax apparent surface radiation temperature). Circled trees focus the surveyed trees selected for the pest and disease trial. 28

Fig. 14. Sony NGRDI orthomosaics for the 2019 season. 29

Fig. 15. Sony MGRVI orthomosaics for the 2019 season. 30

Fig. 16. Sony VDVI orthomosaics for the 2019 season. 31

Fig. 17. Vegetation index maps as derived from multispectral MCAW camera for the 21/07/2019. 33

Fig. 18. Poor correlation of the GM index (left) and the NDCI (right) towards the observed nut damage. The measurements have been labeled by treatment groups C, T1 and T2. 36

Fig. 19. Prediction of *Leaf Anthracosis* using the NGRDI (left) and the MGRVI (right) based on four UAV campaigns. The following symbols were used to label the trees: C2: square; C3: X; C5: plus; T1.2: diamond; T2.3: circle; T2.6: triangle. 38

Fig. 20. Class separability of Bacterial Spot Necrosis by NGRDI (top-left), MGRVI (top-right), VARI (bottom-left) and VDVI (bottom-right). The following symbols were used to label the trees: C2: square; C3: X; C5: plus; T1.2: diamond; T2.3: circle; T2.6: triangle. 39

Fig. 21. Class separability of *Nut Necrosis* by NGRDI (top-left), MGRVI (top-right), VARI (bottom-left) and VDVI (bottom-right). 40

List of Tables

Tab. 1. Sensors mounted on UGV and UAV 15

Tab. 2. Summary of the UAV campaigns performed in the 2019 season. 16

Tab. 3. Vegetation indices tested for the detection of pest and disease infections..... 19

Tab. 4. Processing parameters from Metashape used for orthomosaic generation. 21

Tab. 5. Coefficient of determination and p-value of slope for the linear correlation between various spectral indices based on the Tetracam MCAW-6 orthomosaic of 2019/07/21. Highly significant indices are labeled in bold. 34

Tab. 6. Summary of the linear correlation of various spectral indices to the damaged nuts per branch..... 35

Tab. 7. Correlation of the spectral indices of *Leaf Anthracnosis* based on the four Sony α5100 orthomosaics. 37

Tab. 8. Correlation of the spectral indices to *Leaf Anthracnosis* based on the Tetracam MCAW-6 orthomosaic. 38

Tab. 9. Coherence between *Nut Necrosis* and *Bacterial Spot Necrosis* in the ground truth data of 2019 41

Abbreviations and Acronyms

ANOVA	Standard analysis of variance
API	Application programming interface
Chl _{a+b}	Chlorophyll a+b
CWSI	Crop water stress index
DEM	Digital elevation model
DN	Digital Number
DSM	Digital surface model
ELC	Empirical line claibration
FOV	Field of view
GI	Greenness index
GPS	Global Positioning System
IoT	Internet of Things
MCARI	Modified Chlorophyll Absorption in Reflectance Index
MGRVI	Modified Green Red Vegetation Index
NDCI	Normalised difference chlorophyll index or normalised difference red edge index
NDVI	Normalized differential vegetation index
NGN	Nut gray necrosis
NGRDI	Normalized green red difference index
NIR	Near-infrared
OSAVI	Optimized soil-adjusted vegetation index
PRI	Photochemical reflectance index
RECI	Red edge chlorophyll index
RDVI	Renormalized difference vegetation Index
RGB	Red Green Blue
RGBVI	Red green blue vegetation index
RTK	Real time kinematic
SCADA	Supervisory control and data acquisition
SfM	Structure from motion
SIPI	Structure insensitive pigment index
SR	Simple ratio index
UAV	Unmanned aerial vehicle
UGV	Unmanned ground vehicle
VARI	Visible atmospherically resistant index
VDVI	Visible difference vegetation iIndex
VNIR	Visible and near infrared
WP	Work package
GPS	Global Positioning System
CNN	Convolutional Neural Network

1 Introduction

The aim of this task is to detect possible pest and disease infections within the hazelnut orchard using multispectral remote sensing in the visible to near infrared (VNIR) range and thermal data by the means of unmanned aerial vehicles (UAV) and unmanned ground vehicles (UGV). Insects infestations, mite pests and diseases cause changes in the reflectance properties of leaves, buds, fruits, branches and trunks and should thus be detectable using remote sensing.

Pest- and disease infections in modern orchards present serious threats to farmers as they can result in substantial economic losses and can be deadly in the cases of some fungi or bacteria. Furthermore, disease-sharp and localized application of treatment agents reduce production costs. Early pest and disease recognition is therefore crucial for modern hazelnut farming.

Depending on the disease, the biophysical responses are manifold. They may induce biochemical alterations of the leaves like discoloration, chloroses and structural changes. Mostly affected are the photosynthetic pigments chlorophyll (65%), carotenoids and flavonoids/anthocyanins, as well as xanthophylls [1,2,3]. Xanthophyll pigments also indicate plant stress due to photooxidation under excess insulation [4]. Spectral variations within the blue-green and red part of the visible spectrum (430 to 660nm) occur when stress decreases the chlorophyll content of a plant. Stress may also lead to leaf structural changes, wilting processes and resulting increased dry matter. Such events will decrease absorption in the near-infrared in general, specifically within the water absorption band at 970nm. Several indices for RGB and multispectral regions have successfully been applied for open canopy orchards and UAV applications, and have been summarized in [5,6].

Chlorotic changes have been studied in viticulture for *Flavorescence dorée* and the grapevine leaf disease/Esca complex. Here, the normalized difference vegetation index (NDVI) and other red/NIR, as well as green/red reflectance indices, have shown to correlate well with the occurrence of symptoms and their seasonal development [7,8,9]. In open canopies the underlying soil has a significant influence on the reflectance signal. In the past, indices minimizing the soil background reflectance, such as the Modified CARI (MCARI) and combinations with the Optimized Soil Adjusted Vegetation Index (OSAVI), have proven successful in estimating Chl_{a+b} [10,5]. Calderon et al. [11], achieved early detection of *Verticillium* wilt within an olive orchard by deriving the Crop Water Stress index (CWSI) from thermal imagery. Structural vegetation indices such as the Photochemical Reflectance Index (PRI, [12]) and the blue-green-red-based indices and the Normalized Difference Vegetation Index (NDVI) [13] have been used for damage assessment.

Within the past decade, sensor miniaturization led to the development of numerous operational lightweight sensors for UAV platforms. Imaging hyperspectral sensors at the start of the project were still costly and required more sophisticated processing. Multispectral sensors were thus selected focusing on the visible to near-infrared (NIR) wavelengths (0.4-1 μ m). Thermal remote sensing is supported by broad-band uncooled bolometers detecting thermal radiation between 7-13 μ m. A detailed overview of recent sensors was given by [14].

Analytical methods comprise standard analysis of variance (ANOVA) of reflectances and indices for disease severity classes. Best predictors are then used for classification algorithms like support vector machines, linear discriminant analyses, random forests or neural networks. In a vineyard at the Moselle valley, symptomatic grapevines within the Esca complex and black rot disease were successfully derived from leaf spectrometer measurements at hyperspectral and multispectral levels using random-forest classification TODO (Kafer 2020). [15] applied a convolutional neural network (CNN) method to classify grapevine disease infected canopies and leaves into the classes shadow, ground, healthy and symptomatic parts.

1.1 Deviation from the task description

The PANTHEON consortium has designed several experiments to address its tasks (see Section 2). Unforeseen in the original proposal, the farmer has provided the opportunity to completely cut off some rows of the orchard from irrigation. This allowed for the design of a dedicated water stress experiment. To fully exploit these new opportunities, *Task 4.6 – Water Stress Measurement* has been extended to gain an additional year of data collection. As a byproduct, it can be ensured that trees of the pest and disease experiment—used to produce the results of the given document—are optimally irrigated. In consequence, it is reasonable that the task of separating water stressed trees from trees affected by pest and diseases is shifted from *Task 4.7 – Pest and Disease Detection* to task *T4.6 – Water Stress Measurement*. The resulting increased data availability promises an improved separability between the rapid reactions to water stress and the relatively slow development of damages caused by pests and diseases.

For the given report, spectral indices sensitive to discoloration, pests, and diseases are identified. These are typically also sensitive to other kinds of damages, like water stress. In consequence, the indices identified in the given report will be applied to the experimental sites of *Task 4.6 – Water Stress Measurement*. Along with the information of the thermal UAV camera, which is particularly sensitive to drought stress, the sensitivity of the spectral indices to water stress can be quantified and discriminated.

1.2 Relevant Pests and Diseases

The most important factors causing hazelnut biotic stress are some arthropods (such as mite, coleopteran and heteropteran), phytopathogens fungi, and bacteria. Biotic stress factors considered in the PANTHEON project are:

1. *Phytoptus avellanae* a gall-mite that infests the buds;
2. *Curculio nucum*;
3. True bugs (*Halyomorpha halys*, *Gonocerus acuteangulatus*, *Palomena prasina*, *Piezodorus lituratus*, *Raphygaster nebulosa*, *Nezara viridula* and *Dolycorum baccarum*) involved in the economic detriment due to losses in hazelnut quality caused by kernel abortion, malformation, and the “cimiciato” flavour;



4. *Cytospora* canker, caused by the *ascomycete Cytospora* is involved in apical and complete desiccation of the branch. It can be detected by red dots on tree trunks;
5. *Fusarium lateritium*, a plant pathogen. Causal agent of nut gray necrosis (NGN);
6. The bacteria *Pseudomonas avellanae* and *Xanthomonas arboricola* pv. *Corylina* [16,17].

9

Plant diseases and pest infestation affect plant physiology. This in turn can modify the colour (spectral response) of different parts of the plant, as well as canopy morphology, plant density, transpiration rate, and the interaction of solar and thermal radiation with the canopy [18,19].

Pest infection and plant diseases usually manifest in local symptoms and patches. Therefore, a sound analysis of the spatial variability of spectral indices (see Section 4.1) is expedient to identify diseases. An additional complexity arises from the influence of plant phenology within the growing season on vegetation indices. Structural canopy properties affect spectral indices as well [20]. This prevents the use of fixed pre-selected index thresholds to label pixels as affected by drought or disease. Key for a reliable analysis is a sound standardized image acquisition, since uniform factors such as focus, sharpness, distance between the object and the sensor (pixel size), and illumination are crucial for high accuracy and reproducible results using automated image analysis [21].

2 Experimental setup

2.1 Trials

For pest and disease detection eighteen trees of PANTHEON's Field 18 were selected. Field 18 is characterized by adult trees of the variety *Tonda Gentile Romana* (Nocchione as pollinizers), planted in a 5.0m x 5.0m layout. A sufficient water supply during the season is ensured by an underground drip irrigation line between each planting row.

While diseases are allowed to spread uncontrolled in the area, for the detection of pests a control group C and two infestation groups T1 and T2 were created. Six of the eighteen trees were assigned to each group as illustrated in Fig. 2. The class assignment was performed randomly, while the layout of the eighteen trees was designed to form blocks of two neighbored trees of the same group.

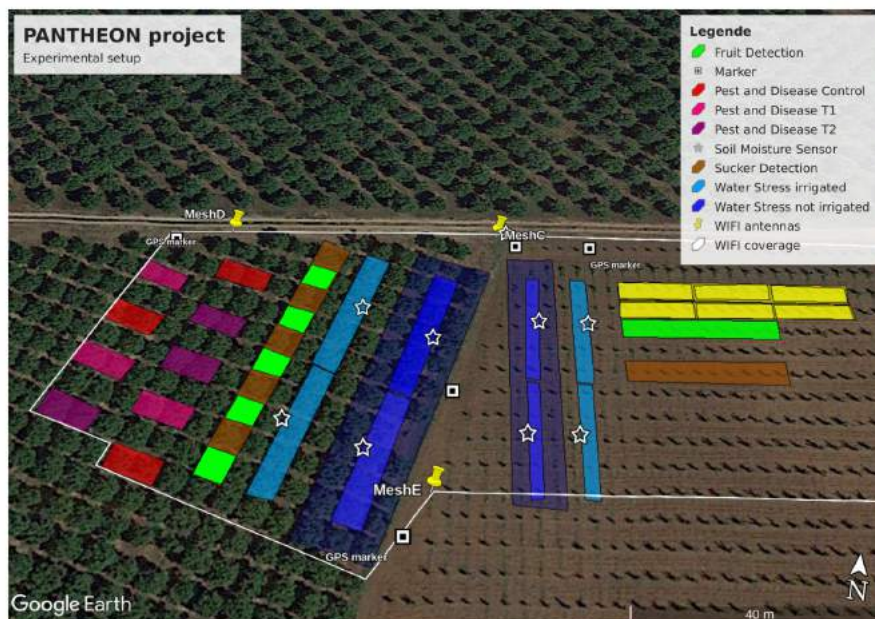


Fig. 1. Overview of the experimental setup of PANTHEON.

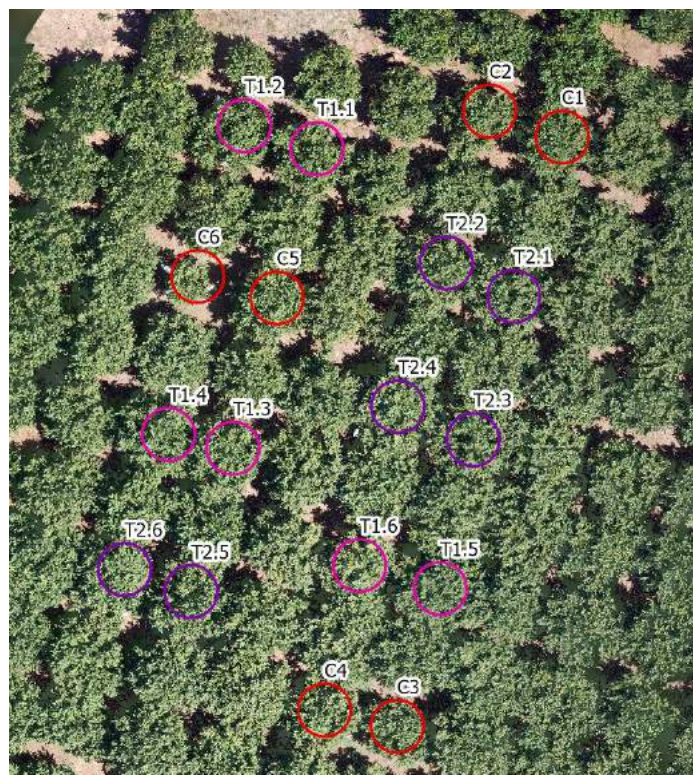


Fig. 2. Detail view of the trees assigned to the pest and disease trials.

For each of the eighteen plants, the five agronomically most important branches were selected by LATUSCIA, each of which should be laterally visible to the UGV and (if possible) vertically visible to the UAV. All branches were protected with handmade cages at the beginning of the trials (see Figure TODO). The cages are composed of a net bag that encloses the apical part of the branch. To have the chance to identify the branches visually in the UAV and UGV images—and to have a spectral

reference for the UGV images—the branches were marked with Styrofoam spheres as illustrated in Fig. 3.

The net bags of treatment group T1 were artificial infested adding true bugs (*Gonocerusacuteangulatus*) on 2019/06/27 by UNITUS. Bugs were placed with the proportion of 1 adult per 5 nuts and were kept in the net bags for one week before removing them. The same procedure was repeated for the plants of group T2 on 2019/07/18. The trees of the control group were not infested.

The *Gonocerusacuteangulatus* is capable of causing the two most impactful kernel damages. If the insects infest the newly developed fruits, they cause kernel abortion and the plant drops the infested fruit (damage detectable on the T1 plants). If the true bugs infest the growing fruit, they cause kernel malformation and an unpleasant nut flavors named *cimiciato* (damage detectable on the T2 plants).



Fig. 3. Branch with Styrofoam sphere and cage (background) and branch of interest marked with sphere (foreground).

2.2 Ground Truth

2.2.1 Pests

During the nut harvest conducted on 2019/09/05, the branches contained by the net bags of the pest and disease trial were cut. The nuts were taken to the laboratory of UNITUS to assess their health status. The nuts were counted and opened, while the number and type of damage of each nut was recorded. In particular, the relative nut damage per branch was calculated. Fig. 4 (left) illustrates the derived portion of damaged nuts for each of the three treatment groups.

The mean value of damaged nuts is about 40% for the control group and about 41% for T2. This indicates a high level of background damage, probably caused by different pests and diseases. A mean value of about 64% for T1, indicates a strong damage caused by the bugs. A one-sided two sample

Student's t-Test confirms that the T1 group has a significantly higher amount of damaged nuts compared to the control group (p-value=0.0024). Statistically, the mean value of the control group C does not differ from the T2 group. This observation allows for the conclusion that the bugs of infestation date T2 were not able to cause significant damage to the nuts. In consequence, differences between the control group and T1 might be detectable using remote sensing techniques, while differences between the control group and T2 would be doubtful.

Fig. 4 (right) illustrates the high inner group and inner tree variability of the damage. Some trees are generally affected by the damage, while for others the nuts of just some branches are damaged. In consequence, if the damage can be identified using remote-sensing, localized damages can be expected.

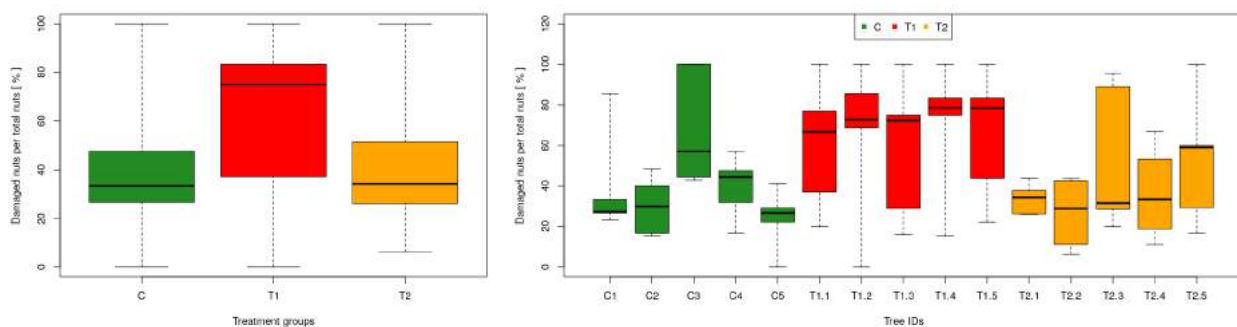


Fig. 4. Boxplots of the ratio of damaged nuts per treatment group (left) and per tree (right). The whiskers extend to the data extremes.

2.2.2 Diseases

Within the pest and disease area, six uniformly spread trees—C2, C3, C5, T1.2, T2.3 and T2.6—were selected (Fig. 2). For each of these trees, samples were taken and analyzed on a seven day basis by UNITUS. The presence of the pathogens was confirmed through isolation of symptoms for each sample. The amount of laboratory work required to quantify each disease limited the number of monitorable plants to the given six trees. In the 2019 season, *Anthracosis* of leaves, *Nut Necrosis* and *Bacterial Spot Necrosis* on bracts and leaves have been monitored. No significant differences in disease quantification, both among plants or between treatment groups (C, T1, T2) were observed by UNITUS. This observation is in line with the experimental setup, since the experiment was designed to control insects, not the spread of diseases.

In addition to the disease monitoring, Dualex measurement of *Flavonoids*, *Chlorophyll*, *Anthocyanin* and *Nitrogen Balance Index* were also taken as control variables.

2.2.2.1 Leaf Anthracosis

Leaf Anthracosis (or *Gleosporiosis*) was the most important disease observed in the PANTHEON orchard during 2019. In the study site the pathogens *Cryptosporiopsis tarraconensis* and *Piggotia coryli* have been observed. For each investigated tree and date of observation, 100 leaves were selected and scanned individually to quantify its necrotic area and pathogen.

Based on these measurements, the average percentage of necrotic leaf area was calculated for each tree and date as illustrated in Fig. 5. In the beginning of the season the observed average necrotic leaf area increases rapidly from about 10 - 15% to a level of about 10 - 20%. From the beginning of July to the beginning of August, the necrotic leaf area increased less dynamically and almost linearly to a level around 15 - 25% for all trees.

Since the leaves develop abundant lesions visible to the human eye, the detection of advanced stage *Leaf Anthracnosis* should be possible with common RGB cameras.

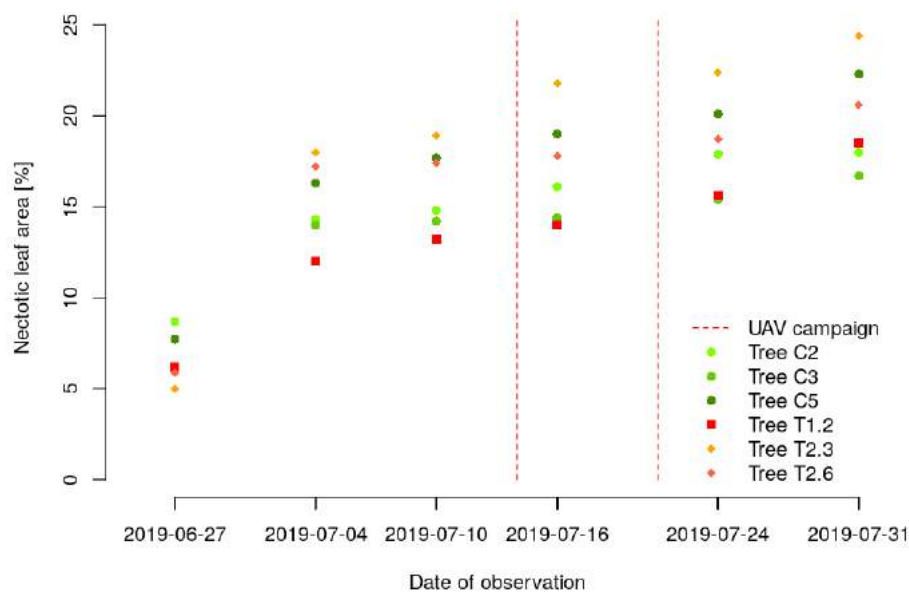


Fig. 5. Nectotic leaf area associated with *Anthracoosis* monitored in PANTHEON test site.

2.2.2.2 Nut Necrosis

Nut Necrosis was visually observed for the selected trees by UNITUS. Six damage classes have been assigned as illustrated in Fig. 6. A slight increase in the presence of symptoms in the 2019 season can be observed. Here, the pathogens *Fusarium lateritium* and *Alternaria alternata* have been identified.

Although *Nut Necrosis* might be detectable with UGV images on individual fruits, the low variability in the study site inhibits an automated detection. As such, a spectral analysis of nut necrosis is not expected to provide any reasonable results at the given stage of the project. An additional season to collect ground truth and remote sensing data might enhance the ability to detect such pathogens. The identification of individual nut clusters in *Task 4.8 – Fruit Detection* might improve the chance to inspect the health of individual fruits.

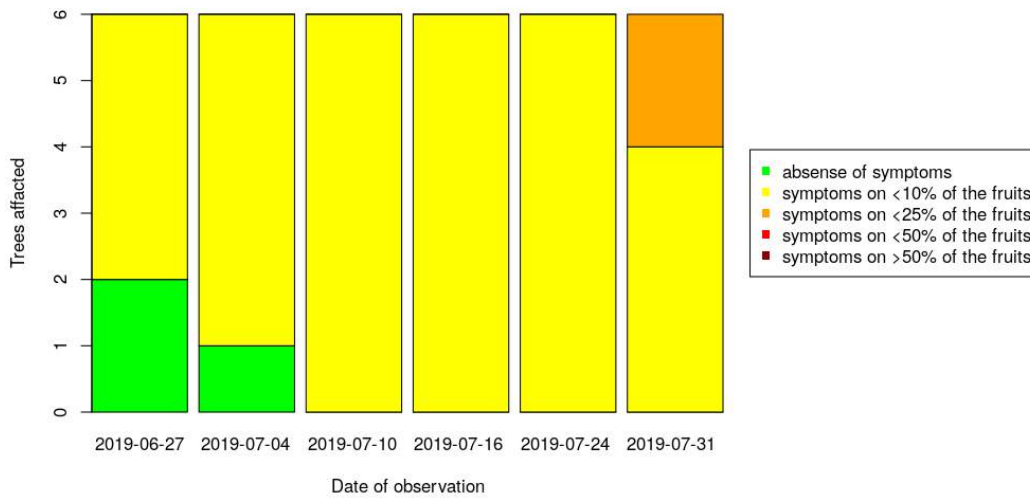


Fig. 6. Development of *Nut Necrosis* on the fruits of the trees over time.

2.2.2.3 Bacterial Spot Necrosis

Bacterial Spot Necrosis has been monitored visually on leaves, bracts, and nuts by UNITUS. The pathogens *Xanthomonas arboricolapv. corylina* and *Sphaceloma coryli* have been observed in the 2019 season. Five damage classes have been assigned as illustrated in Fig. 7. A slight increase in the presence of *Bacterial Spot Necrosis* can be observed for the given trees. To assess its presence and incidence, 50 symptomatic samples (mainly bracts) were collected during each survey. These were stored and transferred to a laboratory for further analysis.

Again, the low variability in the study site inhibits an automated detection of *Bacterial Spot Necrosis* using UAV or UGV data. As such, a spectral analysis of bacterial spot necrosis is not expected to provide any reasonable results without having more variable ground truth data.

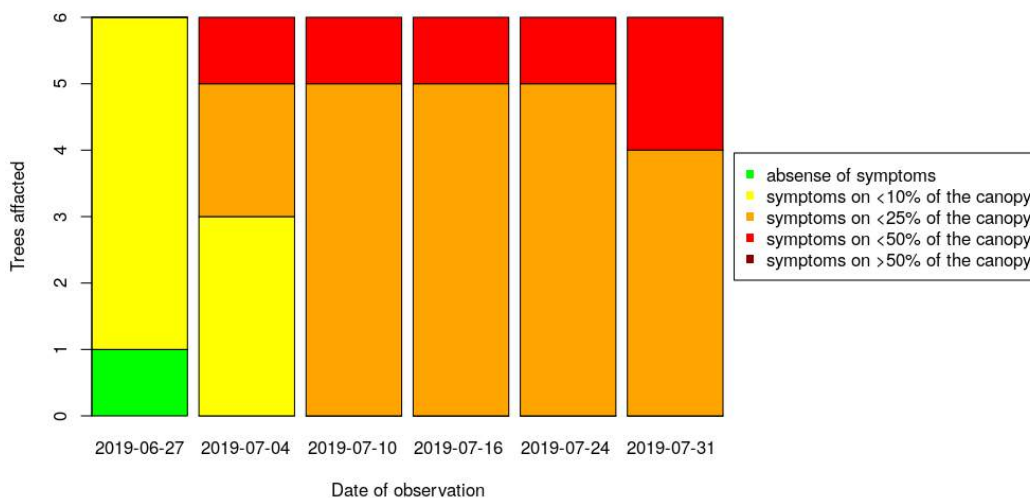


Fig. 7. Development of *Bacterial Spot Necrosis* on the tree canopy over time.

3 Field data

3.1 UAV Campaigns

Three cameras were mounted on the UAV, an RGB camera (Sony α 5100), a customized six-band multi-spectral camera (Tetracam MCAW-6) and a thermal camera (TeAx ThermalCapture-2.0) (Tab. 1). Details can be found in *D4.3 – Aerial Image Processing Pipeline*. For the collection of UAV imagery, the drone was flown at an altitude of about 50 meters and with a speed of about one meter per second.

Band Name	Center Wavelength (nm)	Bandwidth FWHM (nm)
Micasense RedEdge-M (UGV)		
Blue	475	20
Green	560	20
Red	668	10
Near infrared	840	40
Red Edge	717	10
Sony α5100 (UGV,UAV)		
Blue	~400-530	~100
Green	~460-630	~100
Red	~570-700	~130
MCAW (UAV)		
Green	530.7	3
Green-Yellow	550.0	10
Yellow-Green	570.0	10
Red	680.0	10
Red-Edge	720.0	10
Near-infrared	900.0	10
TeAx Thermal Capture 2.0 (UAV)		
Thermal wavelengths	7.5-13.5 μ m	na

Tab. 1. Sensors mounted on UGV and UAV

Seven spectral reference panels were placed next to the field to allow for the conversion of image digital numbers (DNs) to reflectance values, as described in *D4.3 – Aerial Image Processing Pipeline*. The reflectance of each reference panel was measured in the laboratory with a PSR-3500 spectrometer at a spectral resolution of 1nm. These measured reflectances are assumed to remain constant across all UAV campaigns. To facilitate an automated detection of the reference pixels, augmented reality markers with unique IDs corresponding to the reference panels were placed parallel to the panels.

In the 2019 season, seven UAV campaigns were performed by ULB and UNIROMA3. The dates and target areas are based on the tentative data collection plan presented in *Deliverable 2.3 – Real-world (1:1 scale) hazelnut orchard for final demo*. Deviations from the plan are a result of constraints with respect to plant phenology, logistic, and administrative limitations, as well as unforeseen technical

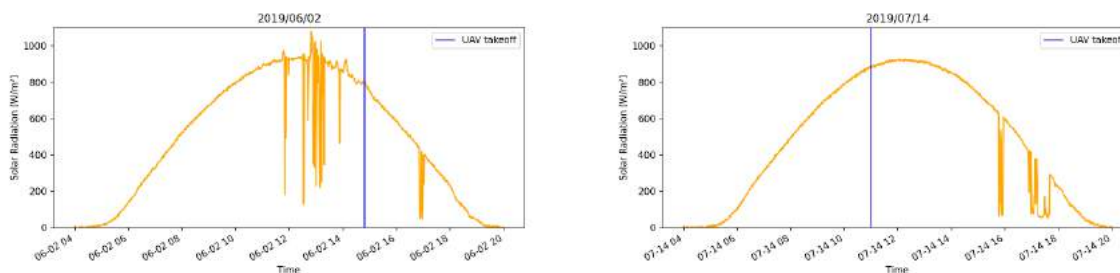
issues. Details on the campaigns can be found in Tab. 2. It needs to be mentioned, that on most days the UAV flew several times to cover different areas of interest.

The data relevant for the given report was collected on four dates (2019/06/02, 2019/07/14, 2019/07/21 & 2019/08/10). Due to problems with calibrating the exposure time of the Tetracam MCAW-6 in the field, all flights after the first pest and disease flight used automatic exposure time settings. Due to an unfortunate technical failure of the Tetracam MCAW-6 on 2019/07/14, only two flights of the MCAW camera were available. The Sony α 5100 RGB camera was functional for all four campaigns.

Date	Fight Areas Covered	Comments
2019/05/11	Water Stress	
2019/06/02	Pest & Disease, Fruit Detection	MCAW overexposed
2019/07/07	Fruit Detection, Water Stress	
2019/07/14	Pest & Disease, Fruit Detection, Water Stress	MCAW failure
2019/07/21	Pest & Disease, Fruit Detection, Water Stress	
2019/08/10	Pest & Disease	no reference panels deployed
2019/08/18	Water Stress	

Tab. 2. Summary of the UAV campaigns performed in the 2019 season.

Fig. 8 illustrates the solar radiation during the relevant UAV campaigns of 2019/06/02, 2019/07/14, 2019/07/21 and 2019/08/10. The solar radiation was measured by the weather station of the experimental site. All campaigns, except for the 2019/08/10, took place at time windows with low cloud coverage and stable illumination conditions.



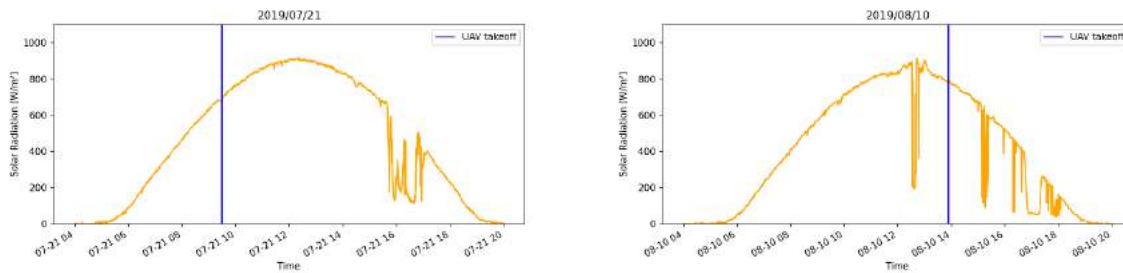


Fig. 8. Solar radiation during the UAV campaigns of 2019/06/02, 2019/07/14, 2019/07/21 and 2019/08/10 measured by the weather station of the field.

3.2 UGV Campaigns

For the remote sensing activities, the UGV has been equipped with a custom RGB camera (Sony α 5100), a five-band multi-spectral camera (MicaSense RedEdge-M) and a laser scanner (Faro Focus S70). In particular, the multi-spectral images are relevant to inspect the potential effect of pests and diseases on the spectral signal. The main objective for collecting terrestrial data was to test, if the presence of pests—and the potentially damaging result of leaves—leads to a spectral response of the branch in general. In particular, a discoloration of the bracts and leaves would make detection possible.

To speed up scans and to simplify the data collection procedure for the agronomists of LATUSCIA, only camera images (Sony α 5100 and MicaSense RedEdge-M) were taken. As such, the standard processing pipeline presented in *D4.2 – Multispectral LiDAR Point Clouds*, which foresees laser scans, was not applicable.

Two UGV campaigns intended for the pest and disease detection were conducted under leave-on conditions. The first campaign was conducted on 2019/08/13, the second on 2019/08/23 as backup. Typically, three trees were selected per target group. One to two selected branches per target tree were captured with the MicaSense RedEdge-M from two different perspectives. The cages were removed right before taking the images. Consequently, six images per treatment group—resulting in a total of 18 images—were collected.

3.3 IoT data

As supplementary measurements, a weather station Terrasense Vantage Pro2 has been installed next to the experimental site. Fig. 9 illustrates the air temperature, air humidity and precipitation during the time window of the ground truth data. In particular the rainfall around the 28th of June might lead to changes between the last date of ground truth data (2019/07/31) and the last UAV campaign (2019/08/10).

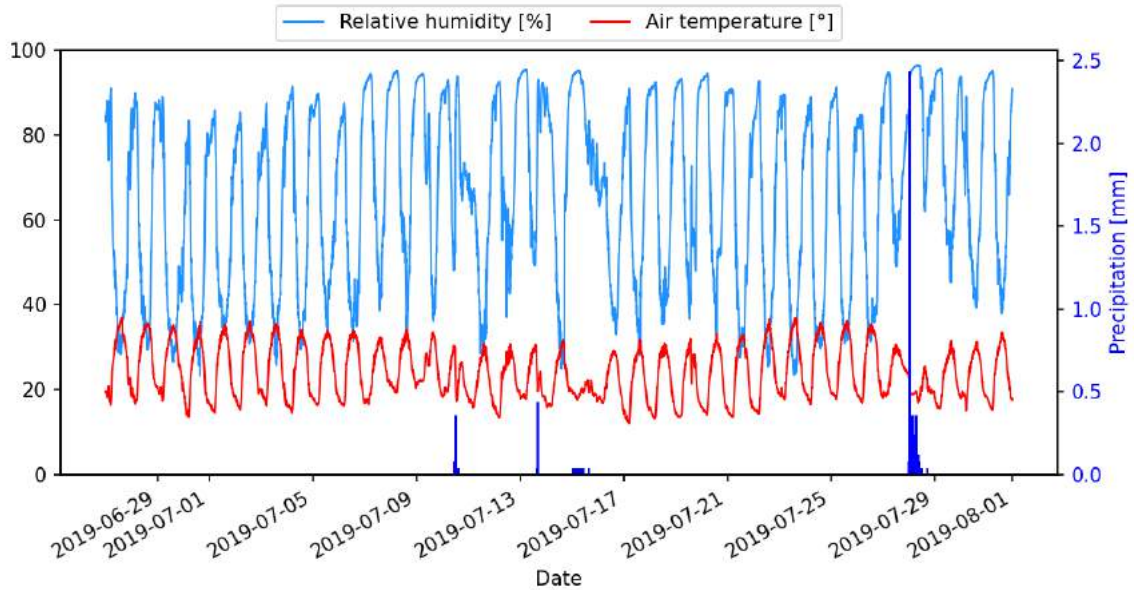


Fig. 9. Environmental conditions during the relevant time period recorded by the IoT network at the study site.

4 Methods

4.1 Vegetation indices

Numerous vegetation indices have been developed in the past decades on different biochemical transactions occurring at the leaf and canopy level. Vegetation indices used for this deliverable focusing on pest and disease detection are summarized in table (Tab. 3).

Index Name	Equation	Reference	Target
Visible			
Normalized Greenness Index/Green Red Vegetation Index	$GI_{norm} = \frac{\rho_{Green} - \rho_{Red}}{\rho_{Green} + \rho_{Red}}$	[22]	Chlorophyll, green biomass
Visible Atmospherically Resistant Index (VARI)	$VARI = \frac{\rho_{Green} - \rho_{Red}}{\rho_{Green} + \rho_{Red} - \rho_{Blue}}$	[23]	Vegetation fraction, vegetation water content/fuel moisture
Visible Difference Vegetation Index	$VDVI = \frac{2 * Green - Red - Blue}{2 * Green + Red + Blue}$	[24]	Green biomass
Modified Green Red Vegetation Index	$MGRVI = \frac{\rho_{Green}^2 - \rho_{Red}^2}{\rho_{Green}^2 + \rho_{Red}^2}$	[6]	Biomass
Red Green Blue Vegetation Index	$RGBVI = \frac{\rho_{Green}^2 - (\rho_{Blue} + \rho_{Red})}{\rho_{Green}^2 + (\rho_{Blue} + \rho_{Red})}$	[6]	Biomass
VISNIR			

Simple Ratio Index	$SR = \frac{\rho_{NIR}}{\rho_{Red}}$	[25]	chlorophyll content vegetation structure, foliage cover; chlorophyll content
Normalized Difference Vegetation Index	$NDVI = \frac{\rho_{NIR} - \rho_{Red}}{\rho_{NIR} + \rho_{Red}}$	[13]	Chlorophyll content, vegetation structure, biomass, LAI
Green NDVI	$GDVI = \frac{\rho_{NIR} - \rho_{Green}}{\rho_{NIR} + \rho_{Green}}$	[26]	Greenness/vitality of vegetation
Renormalized Difference Vegetation Index	$RDVI = \frac{\rho_{NIR} - \rho_{Red}}{\sqrt{\rho_{NIR} + \rho_{Red}}}$	[27]	vegetation structure
Structure Insensitive Pigment Index	$SIPi = \frac{\rho_{NIR} - \rho_{Blue}}{\rho_{NIR} + \rho_{Red}}$	[28]	Chlorophyll and pigments
Red Edge Chlorophyll Index	$RECI = \left(\frac{\rho_{900}}{\rho_{720}} \right) - 1$	[29]	Chlorophyll content
Normalised Difference Chlorophyll Index	$NDCI = \frac{\rho_{900} - \rho_{720}}{\rho_{900} + \rho_{720}}$	[30]	Leaf chlorophyll content
Gitelson and Merzlyak	$GM = \frac{\rho_{720}}{\rho_{550}}$	[31]	Chlorophyll content
Photochemical Reflectance Index	$PRI = \frac{\rho_{531} - \rho_{570}}{\rho_{531} + \rho_{570}}$	[4]	stress-induced changes of chlorophyll/carotenoid ratio, light use efficiency, water stress
Modified Chlorophyll Absorption in Reflectance Index	$MCARI2 = \frac{1.5 * [2.5 * (\rho_{900} - \rho_{680}) - 1.3 * (\rho_{900} - \rho_{550})]}{\sqrt{(2\rho_{900} + 1)^2 - (6\rho_{900} - 5\rho_{670})} - 0.5}$	[32]	Leaf chlorophyll content
Optimized Soil-Adjusted Vegetation Index	$OSAVI = \frac{(1 + 0.16) * (\rho_{900} - \rho_{680})}{\rho_{900} + \rho_{680} + 0.16}$	[33]	vegetation structure, foliage cover, leaf nitrogen, chlorophyll content

Tab. 3. Vegetation indices tested for the detection of pest and disease infections.

4.2 UAV image pre-processing

4.2.1 Tetracam MCAW

Images were exported from the camera in 16-bit TIF format. An empirical line correction (ELC), which assumes a linear relationship between the image DNs and reference panel reflectance, was applied to the Tetracam images [34]. Given a set of representative pixels with known reflectance, the regression coefficients of equation are estimated, allowing for a conversion of pixel DN values to reflectances. The DNs of the reference panels were extracted by automated detection of augmented reality markers. This was performed for each of the six image bands using *Python*. Details can be found in *D4.3 – Aerial Image Processing Pipeline*.

Given that the reference panel reflectance measurements were taken using a higher spectral resolution compared to the Tetracam, reference panel measurements were resampled to the central wavelengths of the Tetracam image bands. As a refinement of the image processing chain, the resampling was performed using the *resample* algorithm from the *propsectr* package in R [35]. In order to integrate the algorithm into the processing pipeline, it was transcribed from *R* into *Python*.

By correlating the reflectance values of each panel with the DNs, a regression line was fitted for each band. Finally, the empirical line was applied to each MCAW image to gain the predicted reflectances for each pixel.

4.2.2 Sony α5100

Except for a file type conversion of the Sony α5100 images, no further image pre-processing was applied. This is motivated by the broad spectral bands, which just allow for the calculation of normalized spectral indices and do not warrant a derivation of reflectance values.

4.2.3 Teax Thermal Camera

Given that the thermal sensor of the Teax ThermalCapture-2.0 records videos rather than producing individual images, small videos are stored by the camera. During post-processing, the first frame of each video is extracted and converted to a .tif file. The DNs of the thermal images are converted to apparent canopy temperatures (T) by applying Equation 1:

$$T = DN * 0.04 - 273.15 \quad (1)$$

4.2.4 Orthomosaic generation

Individual orthomosaics were produced for the Sony α5100, Tetracam MCAW-6, and Teax ThermalCapture-2.0 cameras.

Generating individual orthomosaics—as done for the given report—derives from the processing chain presented in *D4.3 – Aerial Image Processing Pipeline*. It was intended to generate a common geo-referenced orthomosaic for all cameras at once. This procedure failed, since technical problems caused an unsynchronized triggering of the cameras. Consequently, a definite assignment of each image to the RTK GPS positions of the UAV could not be guaranteed. As a mitigation action, the processing chain presented in *D4.3 – Aerial Image Processing Pipeline* has been adapted to be able to process individual orthomosaics without incorporating GPS information.

To produce the results of the given deliverable, geo-referencing of the individual orthomosaics was done manually using a set of aerial orthophotos from the Italian national geoportal. Here, static features located in both the reference orthophotos as well as the orthomosaic were used as control points.

As presented in *D4.3 – Aerial Image Processing Pipeline*, the orthomosaics were generated using Agisoft Metashape [36]. To generate the results for the given report, the parameter set summarized in Tab. 4 was used.

Variable name	Value	Description
Image quality threshold	0.7	Threshold value for the image quality scores calculated by Metashape. Images with quality scores below this value are excluded from orthomosaic processing.
Alignment accuracy	“Highest”	Determines the level of accuracy used to obtain camera position estimates.
Re-projection error threshold	0.3	The threshold for the re-projection error of points within the sparse point cloud. Any points with re-projection error above this value are filtered out.
Reconstruction quality	“Ultra”	Level of quality used for reconstruction of image geometry.
Filtering	“Mild”	Degree of filtering applied to the dense point cloud. Mild is recommended when small details (e.g. tree canopy) are important.
Key points	40000	Maximum number of key points to be generated for each image.
Tie points	0	Maximum number of tie points to be used between images. A value of zero sets an unlimited restriction on the number of tie points.
Blending	“Mosaic”	Determines the method for combining pixel values from different overlapping photos. Mosaic allows for a weighted average, taking into account the distance of each pixel from its image’s center.
Interpolation	“Disabled”	Determines how surface areas without dense cloud points are filled. Disabled allows for accurate reconstruction results as only areas corresponding to dense point clouds are reconstructed.

Tab. 4. Processing parameters from Metashape used for orthomosaic generation.

4.3 UGV image processing

To gain a multi-spectral signal for each captured branch, the individual MicaSense RedEdge-M image bands need to be aligned. The image bands were aligned using a combination of Metashape [36] and OpenCV [37]. For each branch a constant distance to the camera is assumed. Metashape was first used to extract key and tie point coordinates between the image bands. The tie point coordinates were used in OpenCV to determine the homography matrix using the RANSAC algorithm [38]. The homography matrix was then applied to each pixel coordinate in order to warp the projection of the

original image. Although the assumption of a constant distance is hardly true, an approximate projection is derived.

4.4 Feature extraction

For the UAV orthomosaics, the relevant pixels of each target tree were extracted radially around its latitude and longitude coordinates. Given the sampling radius of 1.5 m, the total positional accuracy of the orthomosaic is of minor importance.

For each Tetracam MCAW-6 pixel, the following spectral indices (Tab. 3) were extracted:

- GM
- Greenness
- MCARI2
- NDCI
- NDVI
- OSAVI
- PRI
- RDVI
- RECI
- SR

For each Sony α 5100 pixel, the following spectral indices (Tab. 3) were extracted:

- VDVI
- MGRVI
- NGRDI
- VARI

This procedure has been integrated into PANTHEONs architecture by creating a processing chain. To extract the positions of the trees, to select the relevant orthomosaics, and to join the information with ground measurements, database queries are used. Thus, if new data is available, the features can be calculated and aligned with ground truth data on demand to create new pest and disease predictions.

To extract relevant features for the UGV data, a mask was manually created for each MicaSense RedEdge-M image set (Fig. 10). In addition to labeling the relevant branch, the Styrofoam sphere was also labeled to allow for a spectral normalization of the images.

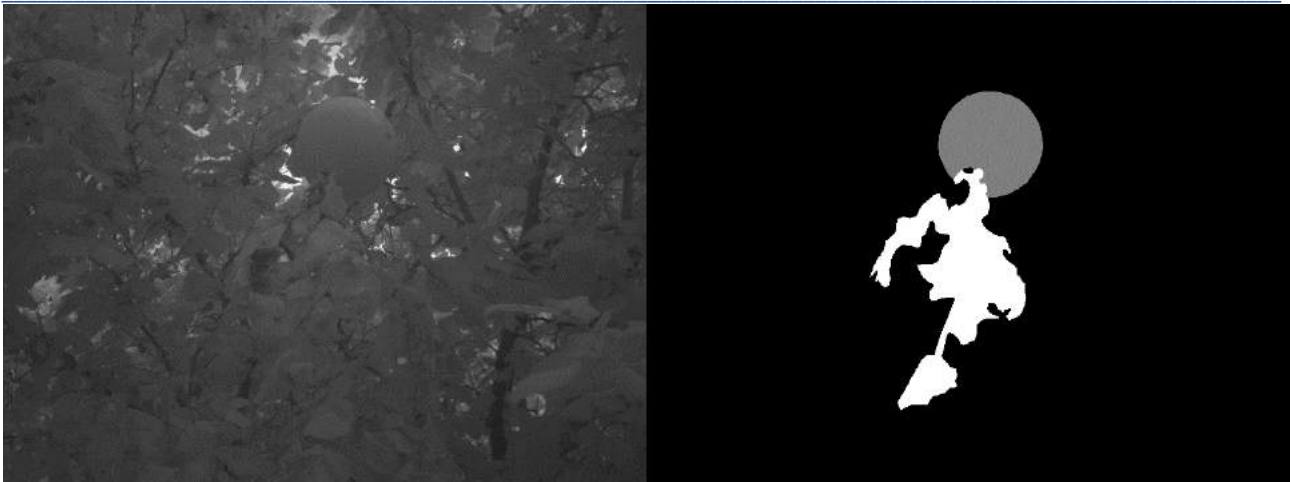


Fig. 10. Single band image from MicaSense RedEdge-M camera (left) and the mask used to determine the target branch pixels (right).

For each MicaSense RedEdge-M image, the following features were extracted:

- GDVI
- GI
- GM
- NDCI
- NDVI
- OSAVI
- RDVI
- RECI
- RGI
- SIPI
- SR
- VARI
- VDVI

4.5 Identification of sensitive indices

A major objective of the pest and disease detection task is to identify spectral indices which are generally sensitive to plant damage, or to a specific disease. Ideally, a linear relationship between the spectral index and a target variable—e.g. portion of damaged nuts per tree—can be observed. For categorical data, ideally the classes should be separable by a threshold of the spectral index. To

increase transferability of the results and ease future data collection, relative indices—not relying on the derivation of reflectance values—are preferred.

To identify sensitive indices for pest detection, the UGV data of the 2019/08/13 was assigned to the ground truth data of the 2019/09/05. The four UAV dates (2019/06/02, 2019/07/14, 2019/07/21 and 2019/08/10) were assigned to the closest temporal disease measurements (2019/06/27, 2019/07/16, 2019/07/24 and 2019/07/31, respectively).

5 Results and Discussion

5.1 UAV processing

5.1.1 Empirical line correction

The empirical correction was successful for the majority of the image bands (Fig. 11). However, due to significant noise in the narrow 530nm band (Fig. 12), the results of the empirical line correction for this specific band were rather poor. To ensure an optimal exposure for vegetation, typically the brightest reference panels are overexposed. Consequently, the overexposed reference panels (typically one per band) were excluded from the ELC, aside from the 900nm band.

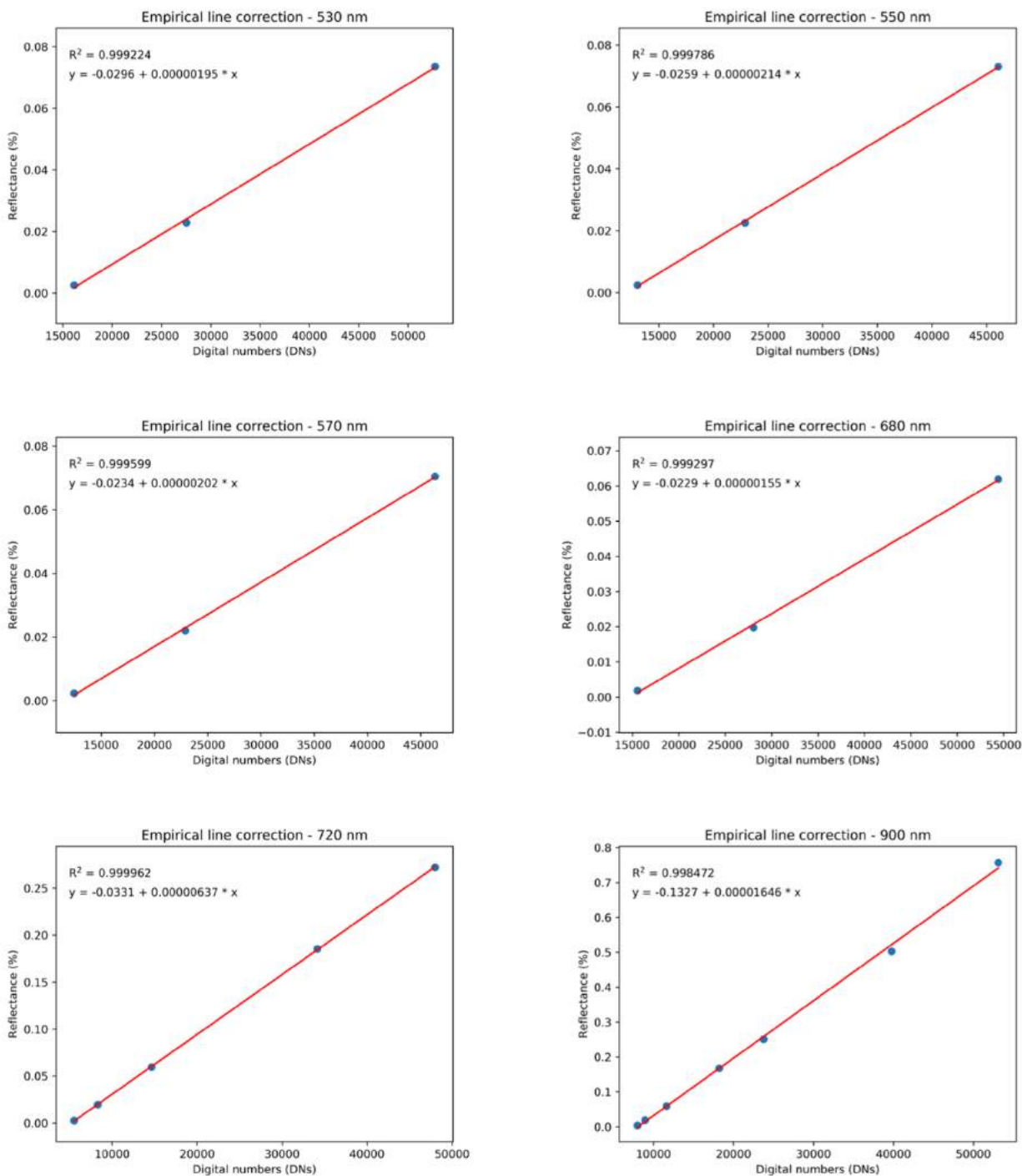


Fig. 11. Results of the empirical line calibration for Tetracam MCAW-6, flight *camp_2019-07-21_09-29-00*.

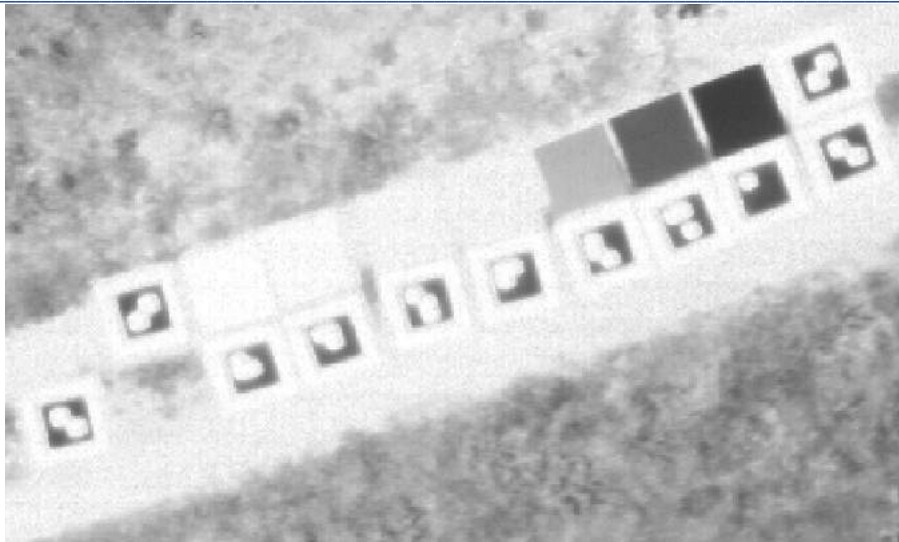


Fig. 12. Noisy band at 530nm for Tetracam MCAW-6 showing the reference panels.

5.1.2 Orthomosaics

Data collected during the flights of 2019/06/02 (4:48 pm.), 2019/07/14 (12:00 am.), 2019/07/21 (10:29 am.) and 2019/08/10 (4:12 pm.) were used to form the orthomosaics from the Sony α 5100 camera. Given that the Tetracam MCAW-6 images taken on 2019/06/02 were highly overexposed and the images of the campaign 2019/08/10 were blurred due to low altitude, only the images from the campaign of 2019/07/21 could be used to form an orthomosaic for the Tetracam MCAW-6 sensor.

For the Tetracam MCAW-6, reflectance images were used, while for the Sony α 5100 and Teax ThermalCapture-2.0 cameras, the raw DN images were used. Images were first filtered based on a quality score from Metashape in order to remove blurry images from orthomosaic construction. Experimentation showed a threshold of 0.7 for the image quality performed best. Any images above this threshold were utilized in the construction of a sparse point cloud, depth maps, and dense point cloud. Tab. 4 shows the settings used for the construction of these three products. Points from the initial sparse point cloud were filtered based on a re-projection error threshold of 0.3 pixels before deriving the depth maps and dense point cloud. From the dense point cloud, a digital elevation model (DEM) was derived. Here, interpolation was deactivated such that only reliable pixels contained data values were utilized. The images were then finally orthomosaiced together using the DEM for orthorectification.

Orthomosaics for the visible, VISNIR and thermal spectral data, as well as the derived vegetation index maps, are illustrated in the appendix. Fig. 13 shows the respective orthomosaics of the 2019/07/21 campaign for the high spatial resolution Sony camera, the multispectral Mcaw data and the apparent surface radiation temperature collected by the Teax thermal camera. During image acquisition irradiation was stable and visibility excellent (Fig. 8).

As images were acquired using automatic exposure setting, a halo of darker hazelnut canopies surrounding the track and reference panels appears in the Sony and multispectral data, which hampers

quantitative analyses regarding the reflectance data. In these areas, the thermal data shows cooler temperatures in the northwestern parts and higher temperatures in the southern/southeastern parts of the pest and disease trial area. Compared to the field data shown in Fig. 5, the T1.2 canopy which features less necrotic leaf area appears cooler, and thus less stressed than T2.3 and C5. On the other side of the study area, the canopy C3 shows the least necrotic area within its canopy, yet the thermal image shows higher apparent canopy temperatures. This could be attributed to water stress and cannot be terminally concluded.

Image acquisition times varied from around noon to afternoon, which is not ideal for seasonal studies as it introduces more error sources such as shadow effects and potential heat stress to plants.

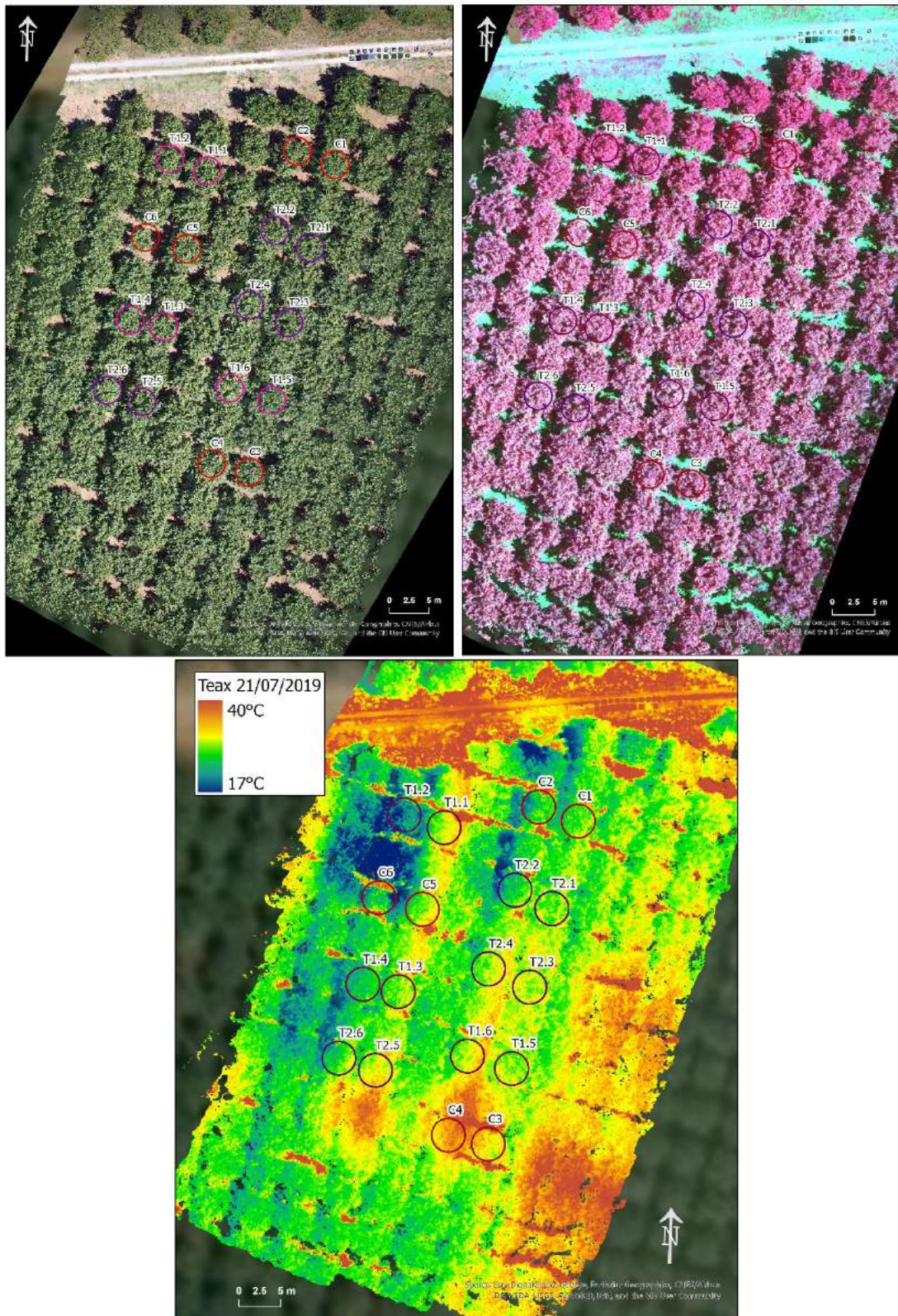


Fig. 13. Orthomosaics from 21 July, 2019 (top-left: Sony RGB, top-right: Mcaw R900nm, G680nm, B550nm, bottom-center: Teax apparent surface radiation temperature). Circled trees focus the surveyed trees selected for the pest and disease trial.

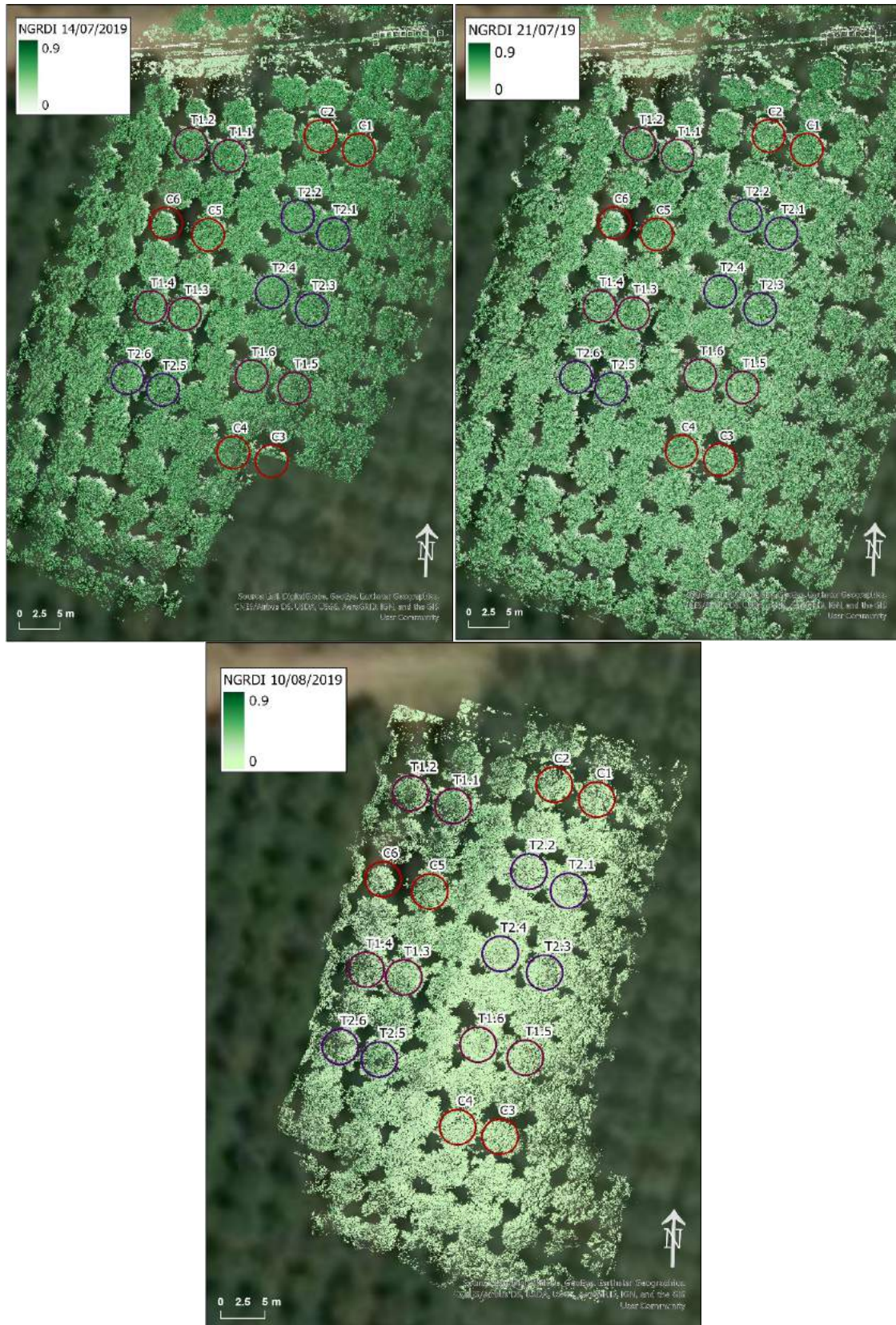


Fig. 14. Sony NGRDI orthomosaics for the 2019 season.



Fig. 16. Sony VDVl orthomosaics for the 2019 season.



The seasonal development for the Sony indices shows decreasing index values, and thus lower amounts of green canopy over the course of the season for the NGRDI (Fig. 14), MGRVI (Fig. 15), and VDVI (Fig. 16) indices. For the MGRVI this effect is especially visible in the southeastern area.

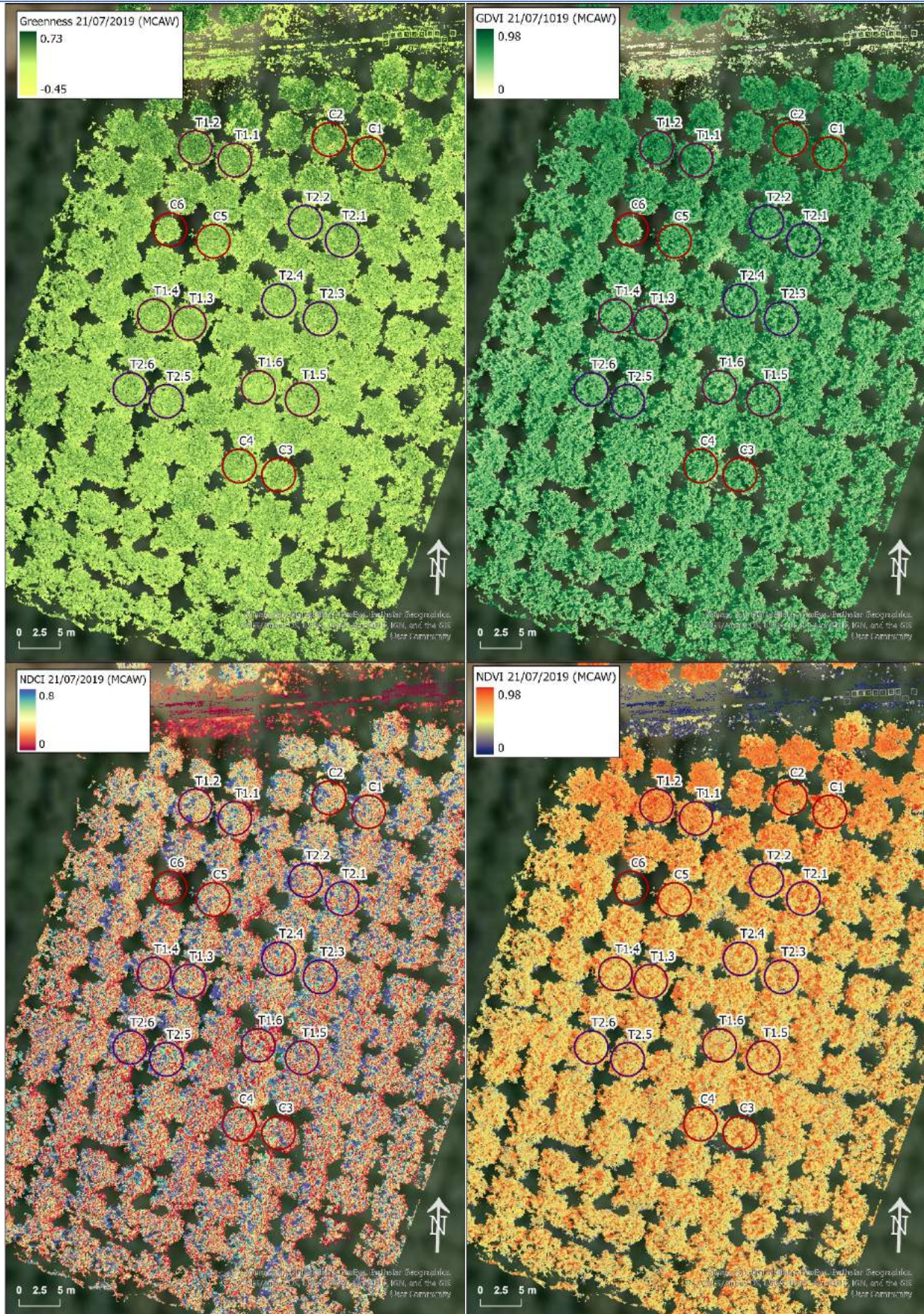


Fig. 17. Vegetation index maps as derived from multispectral MCAW camera for the 21/07/2019

5.2 Sensitivity of spectral indices

5.2.1 Pigments

Tab. 5 summarizes the sensitivity of various spectral indices to the leaf pigments *Chlorophyll*, *Flavonoids*, *Anthocyanin* for the Tetracam MCAW-6 orthomosaic of 2019/07/21. The given results indicate that changes in the *Flavonoids* concentration might be detectable using spectral imagery. The results of *Chlorophyll* and *Anthocyanin* are inconclusive.

Spectral Index	Leaf Pigments R ² (p-value)		
	Chlorophyll	Flavonoids	Anthocyanin
GDVI	0.029 (0.748)	0.728 (0.031)	0.175 (0.410)
GM	0.002 (0.931)	0.526 (0.103)	0.164 (0.425)
Greenness	0.035 (0.723)	0.408 (0.172)	0.073 (0.604)
MCARI2	0.033 (0.729)	0.662 (0.049)	0.177 (0.407)
NDCI	0.245 (0.318)	0.972 (0.000)	0.130 (0.482)
NDVI	0.051 (0.667)	0.734 (0.029)	0.180 (0.402)
OSAVI	0.051 (0.667)	0.734 (0.029)	0.180 (0.402)
PRI	0.215 (0.354)	0.876 (0.006)	0.067 (0.621)
RDVI	0.075 (0.600)	0.000 (0.992)	0.087 (0.570)
RECI	0.277 (0.283)	0.921 (0.002)	0.070 (0.612)
SR	0.060 (0.639)	0.673 (0.045)	0.113 (0.515)

Tab. 5. Coefficient of determination and p-value of slope for the linear correlation between various spectral indices based on the Tetracam MCAW-6 orthomosaic of 2019/07/21. Highly significant indices are labeled in bold.

5.2.2 Pests

Tab. 6 summarizes the results of the correlation between various spectral indices and the amount of damaged nuts per tree. None of the spectral indices have shown to be sensitive to the damage in terms of a significant slope nor a meaningful coefficient of determination. For completeness, Fig. 18 illustrates the poor results of the two best performing spectral indices. These plots also highlight, that no difference between the control group C and the two treatment groups T1 and T2 can be observed.

As the ground truth data already has highlighted, the damages caused by buds are very localized (see Section 2.2.1). No spectral response of the branches could be observed in either the visible spectrum or near infrared region. These results suggest that, if damages lead to a spectral response at all, this will be limited to the fruit level only. In consequence, a prior detection of individual nuts or clusters—as strived for in *Task 4.8 – Fruit Detection*—would be required for a further analysis.

Spectral Index	Number of supporting measurements (N)	Significance of slope (p-value)	Coefficient of determination (R²)
GDVI	17	0.707	0.010
GI	17	0.789	0.005
GM	17	0.325	0.065
NDCI	17	0.340	0.061
NDVI	17	0.835	0.003
OSAVI	17	0.835	0.003
RDVI	17	0.928	0.001
RECI	17	0.381	0.052
RGI	17	0.744	0.007
SIPI	17	0.889	0.001
SR	17	0.821	0.004
VARI	17	0.815	0.004
VDVI	17	0.677	0.012

Tab. 6. Summary of the linear correlation of various spectral indices to the damaged nuts per branch.

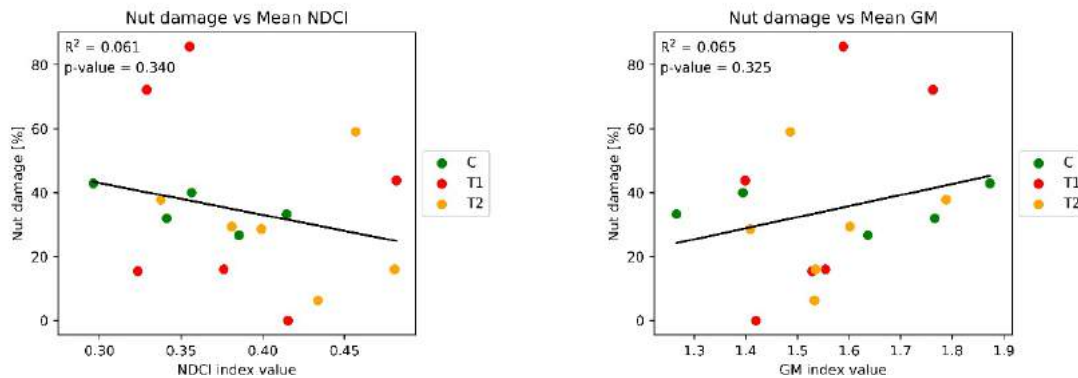


Fig. 18. Poor correlation of the GM index (left) and the NDCI (right) towards the observed nut damage. The measurements have been labeled by treatment groups C, T1 and T2.

5.2.3 Leaf anthracnosis

Tab. 7 summarizes the correlation of all spectral indices applied to the Sony $\alpha 5100$ orthomosaics of the 2019/06/02, 2019/07/14, 2019/07/21 and 2019/08/10 flights. In terms of the coefficient of determination, the NGRDI resulted in an R^2 value of 0.65, the best correlation with *Leaf Anthracnosis*. With a p-value close to zero the slope of the regression line differs highly significantly from zero. The MGRVI showed a similar performance, with an R^2 value of 0.61. Accordingly, Fig. 19 illustrates the linear regression lines of the two best performing indices, NGRDI and MGRVI, to predict *Leaf Anthracnosis*.

From completeness, Tab. 7 also provides the R^2 values and p-values for individual trees. This data has been derived, to identify trees whose damage might be systematically under- or over-predicted by the indices.

Spectral Index	Tree	Number of supporting measurements (N)	Significance of slope (p-value)	Coefficient of determination (R^2)
VDVI	all	24	0.000	0.457
	C2	4	0.005	0.991
	C3	4	0.010	0.980
	C5	4	0.349	0.424
	T1.2	4	0.685	0.099
	T2.3	4	0.056	0.892

	T2.6	4	0.239	0.580
MGRVI	all	24	0.000	0.614
	C2	4	0.021	0.958
	C3	4	0.065	0.874
	C5	4	0.132	0.753
	T1.2	4	0.176	0.679
	T2.3	4	0.002	0.996
	T2.6	4	0.053	0.896
NGRDI	all	24	0.000	0.645
	C2	4	0.025	0.950
	C3	4	0.035	0.932
	C5	4	0.102	0.806
	T1.2	4	0.160	0.706
	T2.3	4	0.003	0.994
	T2.6	4	0.037	0.928
VARI	all	24	0.000	0.469
	C2	4	0.055	0.893
	C3	4	0.207	0.629
	C5	4	0.227	0.598
	T1.2	4	0.330	0.449
	T2.3	4	0.031	0.938
	T2.6	4	0.069	0.867

Tab. 7. Correlation of the spectral indices of *Leaf Anthracnosis* based on the four Sony α 5100 orthomosaics.

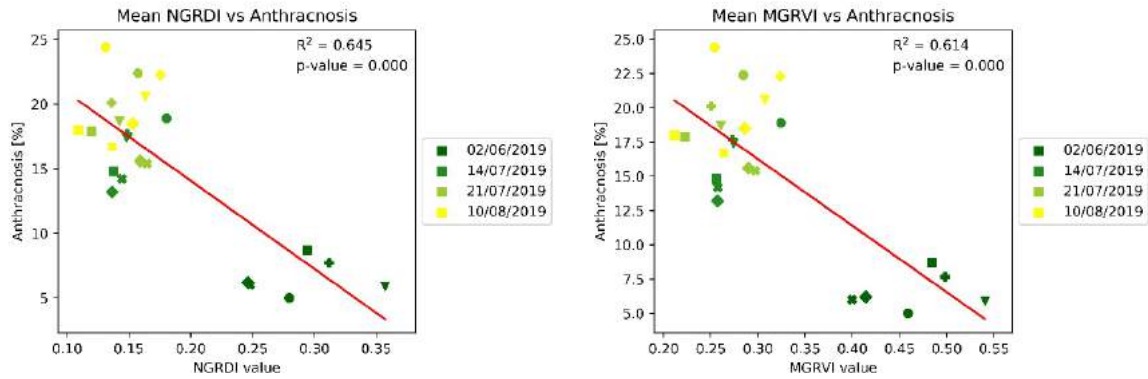


Fig. 19. Prediction of *Leaf Anthracnosis* using the NGRDI (left) and the MGRVI (right) based on four UAV campaigns. The following symbols were used to label the trees: C2: square; C3: X; C5: plus; T1.2: diamond; T2.3: circle; T2.6: triangle.

Tab. 8 summarizes the correlation between various spectral indices of the Tetracam MCAW-6 orthomosaic (2019/07/21) and *Leaf Anthracnosis*. Due to the limited amount of data, low variability in the field, and automatic exposure settings, no spectral index sensitive to *Leaf Anthracnosis* could be identified.

Spectral Index	Number of supporting measurements (N)	Significance of slope	Coefficient of determination (R ²)
GDVI	6	0.272	0.288
GM	6	0.211	0.356
Greenness	6	0.380	0.196
MCARI2	6	0.349	0.220
NDCI	6	0.684	0.046
NDVI	6	0.360	0.211
OSAVI	6	0.360	0.211
PRI	6	0.629	0.064
RDVI	6	0.558	0.092
RECI	6	0.700	0.043
SR	6	0.325	0.239

Tab. 8. Correlation of the spectral indices to *Leaf Anthracnosis* based on the Tetracam MCAW-6 orthomosaic.

5.2.4 Bacterial spot necrosis

Fig. 20 summarizes the sensitivity of the spectral indices on *Bacterial Spot Necrosis* based on the Sony $\alpha 5100$ orthomosaics of the 2019/06/02, 2019/07/14, 2019/07/23 and 2019/08/10 flights. Low damage classes (0 and 1) can be separated well from high damage classes (2 and 3) using a NGRDI threshold of e.g. 0.2 or a MGRVI thresholds of e.g. 0.35. However, since the early flight of 2019/06/02 is the only data set providing ground truth information for the low damage classes, the significance of the results is limited without collecting additional data.

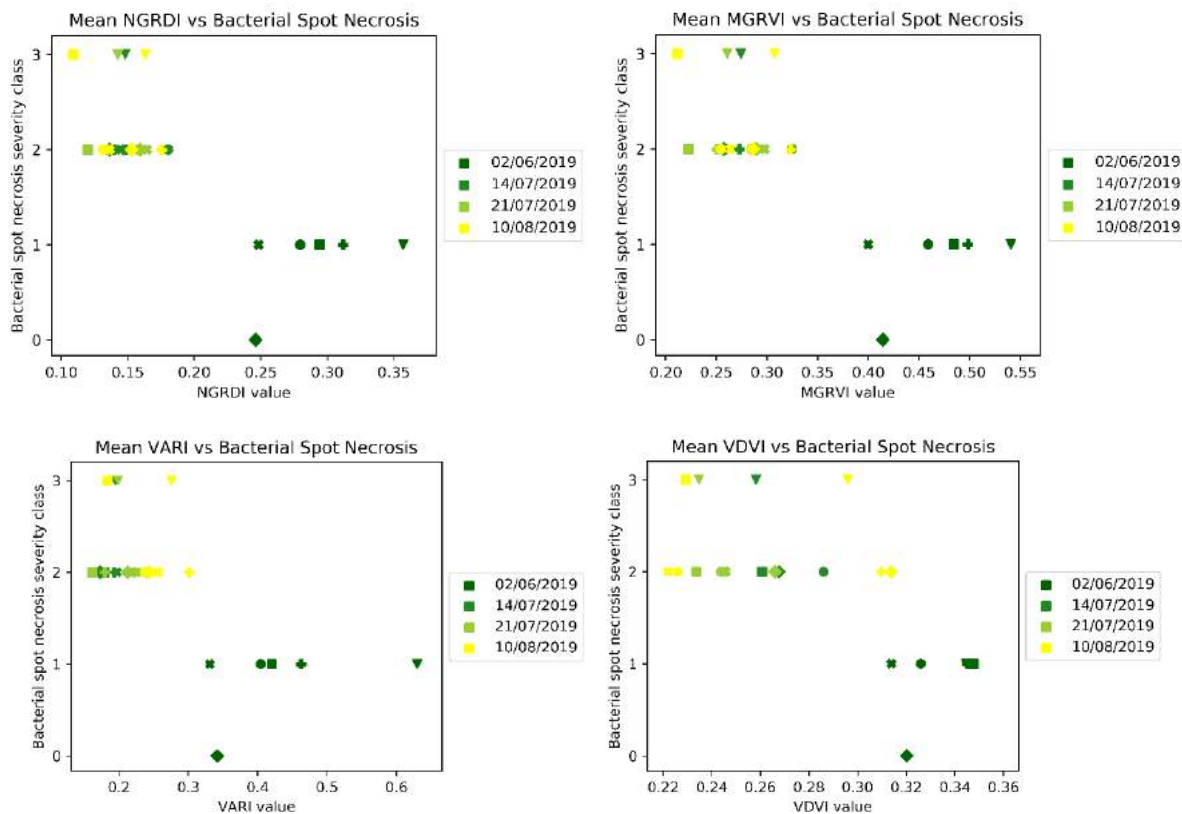


Fig. 20. Class separability of Bacterial Spot Necrosis by NGRDI (top-left), MGRVI (top-right), VARI (bottom-left) and VDMI (bottom-right). The following symbols were used to label the trees: C2: square; C3: X; C5: plus; T1.2: diamond; T2.3: circle; T2.6: triangle.

5.2.5 Nut necrosis

Fig. 21 summarizes the sensitivity of the spectral indices with regards to *Nut Necrosis* based on the Sony $\alpha 5100$ orthomosaics of the 2019/06/02, 2019/07/14, 2019/07/21 and 2019/08/10. Compared to *Bacterial Spot Necrosis*, the severity classes are poorly separable by the spectral indices. This effect is not unexpected, since *Nut Necrosis* results in localized damages of the fruits hardly detectable using aerial data.

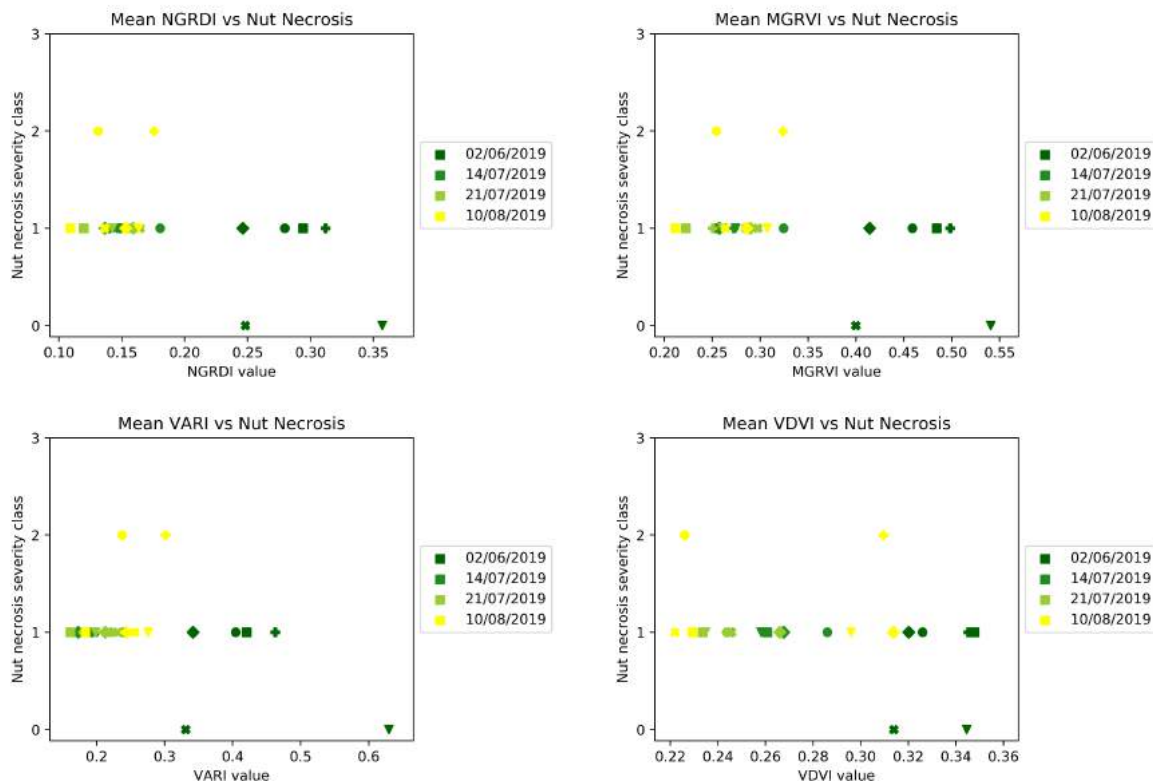


Fig. 21. Class separability of *Nut Necrosis* by NGRDI (top-left), MGRVI (top-right), VARI (bottom-left) and VDVI (bottom-right).

5.2.6 General Discussion

As the results for *Leaf Anthracnosis*, *Bacterial Spot Necrosis* and *Nut Necrosis* show, the spectral indices are sensitive to discoloration in general. Consequently, the best performing indices are sensitive to multiple diseases and pathogens.

Tab. 9 illustrates the coherence between *Nut Necrosis* and *Bacterial Spot Necrosis* in the ground truth data of 2019. For the observed trees there is a notable correlation in the occurrence of *Bacterial Spot Necrosis* and *Nut Necrosis*. Thus, the spectral indices are likely to be sensitive to both diseases, even if the spectral response is just caused by a particular disease. As such, the spectral indices identified in the given report show to be sensitive to the ground truth data of season 2019 in general but can not to be seen as a predictor for a specific disease.

		Nut Necrosis				
		Absence of symptoms	symptoms on <10% of the fruits	symptoms on <25% of the fruits	symptoms on <50% of the fruits	symptoms on >50% of the fruits
Bacterial Spot Necrosis	Absence of symptoms	0	1	0	0	0
	symptoms on <10% of the canopy	2	6	0	0	0
	symptoms on <25% of the canopy	0	19	2	0	0
	symptoms on <50% of the canopy	1	5	0	0	0
	symptoms on >50% of the canopy	0	0	0	0	0

Tab. 9. Coherence between *Nut Necrosis* and *Bacterial Spot Necrosis* in the ground truth data of 2019

6 Conclusions

The given document summarizes the methodology for *Task 4.5 – Pest and Disease Detection*. The data pre-processing chains for the different data sources of UGV and UAV have been described. Based on the platform and data availability, different absolute and relative spectral indices have been derived. The sensitivity of the spectral indices towards typical pests and diseases present in the PANTHEON orchard have been tested for the 2019 season.

During the 2019 season, a designated experiment for pest detection has been conducted. It was attempted to assess the damage caused by true bugs by means of spectral analysis of the trees at the individual branch level. Using multispectral UGV imagery, no significant spectral response on the branch level could be identified.

The most common diseases in the 2019 season—*Leaf Anthracnosis*, *Bacterial Spot Necrosis* and *Nut Necrosis*—were addressed using various spatial indices using UAV imagery. Relative spectral indices of the visible range, like the NGRDI and the MGRVI, have shown to be sensitive to *Leaf Anthracnosis* as well as *Bacterial Spot Necrosis*.

6.1 Completed tasks

The methodology for *Task 4.5 – Pest and Disease Detection* has been developed and implemented. The algorithms presented in *D4.3 – Aerial Image Processing Pipeline* have been adapted to provide orthomosaics for each UAV camera individually. Processing chains have been implemented to allow for a semi-automated analysis of the spectral features. These scripts exploit PANTHEONs database structure to fuse the spectral measurements, IoT measurements and ground truth data using database queries. In particular, soil moisture and temperature, as well as air temperature and humidity can be linked to each tree. In this way, suitable spectral indices for identifying damages—probably caused

by pests and diseases—can be identified on demand as soon as new data is available. The processing chains also create orthomosaic images of the spectral indices or damage severity maps as a basis to inspect time series of specific hazelnut trees.

A prior analysis of the UAV and UGV data collected in the 2019 season has been conducted. Due to the flexible structure allowed by the database, alternative empirical models to identify pests and disease and distinguish them from water stress can be easily implemented. In particular, with the given implementation, the pest and disease detection can be seen as a database application.

6.2 Future Research

The disappointing results of the pest detection using UGV images lead to the conclusion, that the damages caused by pests (true bugs) are too localized to be detected on individual branch level. It needs to be noted, that the presented approach to extract pixels belonging to specific branches is prone to errors. Notably, a misalignment of the image bands may lead to distortion of the spectral indices. However, the sensitivity of the correlations was too poor to expect an improvement by merely improving the band alignment.

A promising alternative approach to detecting pests and *Nut Necrosis* could be a spectral analysis on the level of individual fruits or clusters. After the completion of *Task 4.8 – Fruit Detection*, an automated spectral analysis of individual clusters is imaginable. Therefore, an extraction of the spectral response from the upcoming fruit detection is considered. To achieve this goal, the spectral response extracted from the images used for fruit detection needs to be linked to the trees and stored in the database. Using this approach, a spectral analysis of the detected fruits could be achieved using database queries.

The ground truth data for *Nut Necrosis* (see Section TODO) and *Bacterial Spot Necrosis* (see Section TODO) of the 2019 season have shown to be too invariable to allow for a reasonable automated disease classification. An additional season of data collection is expected to improve the availability and usefulness of ground truth data. Therefore, the data collected in the 2020 season is planned to be used for a further analysis.

6.3 Criticalities and Mitigation Actions

At the time of submitting the given document, the opportunities to analyze the pest and disease data are limited. Due to unforeseeable administrative (restricted flight area) and technical difficulties (camera failure, interference of antennas), as well as unsuitable camera settings (exposure time, focus), the amount of high-quality UAV data was not optimal. Additionally, the unexpectedly low occurrence of diseases in the orchard and its low variability hampered an extensive analysis. In particular, methods to classify between *healthy* and *diseased* trees are not reasonably applicable yet. Thus, an additional seasonal data is required for an assessment of validation measure C as presented in deliverable *D4.1 – Requirements, Specifications and Benchmark*. It is planned to be validated at the end of *Task 4.5 – Pest and Disease Detection*.

Most of the diseases typical in PANTHEONs hazelnut orchard develop beginning from early spring. Due to administrative and logistic reasons, the ground truth data collection started at end of June in 2019. In addition, due to technical constraints, the UAV campaigns of 2019 also started at the beginning of June. Thus, a critical timeframe to identify diseases in their early stages could not be investigated in season 2019.

Due to the unfortunate occurrence of the COVID-19 pandemic in March 2020, the collection of ground truth data as well as the collection of UAV data is hampered. In particular, the critical phase at begin of the season is missing again. Therefore, the 2021 season should serve as relevant additional data for a proper final analysis of pests and diseases in the PANTHEON area.

In the 2019 season, a high temporal difference between the collection of the first and last dates of ground truth data and the corresponding UAV flights occurred. Due to the dynamic development of diseases in the orchard, these temporal offsets are expected to have negatively affected the results of the given report. To improve the accuracy and significance of the models, a simultaneous collection of ground truth and sensor data should be strived for.

In future UAV campaigns, emphasis on ensuring excellent image quality—image sharpness, optimal exposure—is necessary. This will help to increase the quality of the empirical line correction, as well as the orthomosaics in general. The data collection routines have been revised and simplified to ease and optimize the UAV setup in the field. In particular, the data collected in the 2019 season has been used to calibrate a lookup table, allowing the selection of a proper fixed exposure time in the field by taking advantage of the solar radiation measurements of the weather station.

The implementation of a dedicated water stress experiment with the extension of *Task 4.6 – Water Stress Measurement* has provided the opportunity to collect an additional season of data for water stress detection. Since drought stress, like other kinds of damage, leads to a discoloration of leaves, spectral indices sensitive to diseases are typically also sensitive to water stress. Thus, to distinguished between water stress and pests or diseases, indices sensitive to water stress need to be identified first before the effects can be distinguished. In particular, the thermal images of the Teax ThermalCapture-2.0 are a promising tool to detect rapidly reacting water stress in an early stage. Deviating from the original task description, the decorrelation between pests or diseases and water stress has been shifted to *Task 4.6 – Water Stress Measurement*. The results will be incorporated in a later stage of *Task 4.5 – Pest and Disease Detection*.

6.4 Ongoing activities

As the timeline of *Task 4.7 – Pest and Disease Detection* foresees, with the submission of the given deliverable the collection of remote sensing and ground truth data is not yet complete. In particular, the methods presented in the given document will be applied on new UAV data once available. A refinement of the representation of the outputs, e.g. damage severity maps, will be conducted in close cooperation with *Task 5.4 – Major diseases Monitoring and Control*. The selection and application of further statistical models will be conducted depending on the data availability.

7 References

- [1] G. Guyot, "Optical properties of vegetation canopies.," *Opt. Prop. Veg. canopies.*, pp. 19–43, 1990.
- [2] F. Kurz, "Lehrstuhl für Photogrammetrie und Fernerkundung Schätzung von Vegetationsparametern aus multispektralen Fernerkundungsdaten," 2003.
- [3] H. G. Jones and R. A. Vaughan, *Remote Sensing of Vegetation: Principles, Techniques, and Applications*. Oxford: Oxford University Press, 2010.
- [4] J. A. Gamon, L. Serrano, and J. S. Surfus, "The photochemical reflectance index: An optical indicator of photosynthetic radiation use efficiency across species, functional types, and nutrient levels," *Oecologia*, vol. 112, no. 4, pp. 492–501, Dec. 1997.
- [5] P. J. Zarco-Tejada, J. R. Miller, A. Morales, A. Berjón, and J. Agüera, "Hyperspectral indices and model simulation for chlorophyll estimation in open-canopy tree crops," *Remote Sens. Environ.*, vol. 90, no. 4, pp. 463–476, Apr. 2004.
- [6] J. Bendig *et al.*, "Combining UAV-based plant height from crop surface models, visible, and near infrared vegetation indices for biomass monitoring in barley," *Int. J. Appl. Earth Obs. Geoinf.*, vol. 39, pp. 79–87, Jul. 2015.
- [7] S. F. di Gennaro *et al.*, "Unmanned Aerial Vehicle (UAV)-based remote sensing to monitor grapevine leaf stripe disease within a vineyard affected by esca complex," *Phytopathol. Mediterr.*, vol. 55, no. 2, pp. 262–275, Jul. 2016.
- [8] J. Albetis *et al.*, "Detection of Flavescence dorée Grapevine Disease Using Unmanned Aerial Vehicle (UAV) Multispectral Imagery," *Remote Sens.*, vol. 9, no. 4, p. 308, Mar. 2017.
- [9] J. Albetis *et al.*, "On the Potentiality of UAV Multispectral Imagery to Detect Flavescence dorée and Grapevine Trunk Diseases," *Remote Sens.*, vol. 11, no. 1, p. 23, Dec. 2018.
- [10] D. Haboudane, J. R. Miller, N. Tremblay, P. J. Zarco-Tejada, and L. Dextraze, "Integrated narrow-band vegetation indices for prediction of crop chlorophyll content for application to precision agriculture," *Remote Sens. Environ.*, vol. 81, no. 2–3, pp. 416–426, Aug. 2002.
- [11] R. Calderón, M. Montes-Borrego, B. B. Landa, J. A. Navas-Cortés, and P. J. Zarco-Tejada, "Detection of downy mildew of opium poppy using high-resolution multi-spectral and thermal imagery acquired with an unmanned aerial vehicle," *Precis. Agric.*, vol. 15, no. 6, pp. 639–661, Oct. 2014.
- [12] J. A. Gamon, J. Peñuelas, and C. B. Field, "A narrow-waveband spectral index that tracks diurnal changes in photosynthetic efficiency," *Remote Sens. Environ.*, vol. 41, no. 1, pp. 35–44, Jul. 1992.
- [13] J. W. Rouse, R. H. Haas, J. A. Schell, and D. W. Deering, "Monitoring vegetation systems in the Great Plains with ERTS." 1973.
- [14] H. Aasen, E. Honkavaara, A. Lucieer, and P. Zarco-Tejada, "Quantitative Remote Sensing at Ultra-High Resolution with UAV Spectroscopy: A Review of Sensor Technology, Measurement Procedures, and Data Correction Workflows," *Remote Sens.*, vol. 10, no. 7, p. 1091, Jul. 2018.
- [15] M. Kerkech, A. Hafiane, and R. Canals, "Vine disease detection in UAV multispectral images using optimized image registration and deep learning segmentation approach," *Comput. Electron. Agric.*, vol. 174, p. 105446, Jul. 2020.

- [16] M. Scortichini, "LE PRINCIPALI AVVERSITA' DEL NOCCIOLO NEL LAZIO," 2006.
- [17] J. R. Lamichhane, C. Bartoli, and L. Varvaro, "Extensive Field Survey, Laboratory and Greenhouse Studies Reveal Complex Nature of *Pseudomonas syringae*-Associated Hazelnut Decline in Central Italy," *PLoS One*, vol. 11, no. 2, Feb. 2016.
- [18] G. L. Hartman, E. D. West, and T. K. Herman, "Crops that feed the World 2. Soybean-worldwide production, use, and constraints caused by pathogens and pests," *Food Secur.*, vol. 3, no. 1, pp. 5–17, Mar. 2011.
- [19] M. Gerhards, G. Rock, M. Schlerf, and T. Udelhoven, "Water stress detection in potato plants using leaf temperature, emissivity, and reflectance," *Int. J. Appl. Earth Obs. Geoinf.*, vol. 53, pp. 27–39, Dec. 2016.
- [20] R. Hernández-Clemente, R. M. Navarro-Cerrillo, L. Suárez, F. Morales, and P. J. Zarco-Tejada, "Assessing structural effects on PRI for stress detection in conifer forests," *Remote Sens. Environ.*, vol. 115, no. 9, pp. 2360–2375, Sep. 2011.
- [21] A. K. Mahlein, "Plant disease detection by imaging sensors – Parallels and specific demands for precision agriculture and plant phenotyping," *Plant Disease*, vol. 100, no. 2. American Phytopathological Society, pp. 241–254, 01-Feb-2016.
- [22] C. J. Tucker, "Red and photographic infrared linear combinations for monitoring vegetation," *Remote Sens. Environ.*, vol. 8, no. 2, pp. 127–150, May 1979.
- [23] A. A. Gitelson, Y. J. Kaufman, R. Stark, and D. Rundquist, "Novel algorithms for remote estimation of vegetation fraction," *Remote Sens. Environ.*, vol. 80, no. 1, pp. 76–87, Apr. 2002.
- [24] X. Wang, M. Wang, S. Wang, and Y. Wu, "Extraction of vegetation information from visible unmanned aerial vehicle images," *Nongye Gongcheng Xuebao/Transactions Chinese Soc. Agric. Eng.*, vol. 31, no. 5, pp. 152–159, Mar. 2015.
- [25] C. J. Tucker and P. J. Sellers, "Satellite remote sensing of primary production," *Int. J. Remote Sens.*, vol. 7, no. 11, pp. 1395–1416, 1986.
- [26] W. Wu, "The Generalized Difference Vegetation Index (GDVI) for dryland characterization," *Remote Sens.*, vol. 6, no. 2, pp. 1211–1233, Feb. 2014.
- [27] J. L. Roujean and F. M. Breon, "Estimating PAR absorbed by vegetation from bidirectional reflectance measurements," *Remote Sens. Environ.*, vol. 51, no. 3, pp. 375–384, Mar. 1995.
- [28] J. Penuelas, "Semi-empirical indices to assess carotenoids/chlorophyll a ratio from leaf spectral reflectance," *Photosynthetica*, vol. 31, pp. 221–230, 1995.
- [29] A. A. Gitelson, Y. Gritz, and M. N. Merzlyak, "Relationships between leaf chlorophyll content and spectral reflectance and algorithms for non-destructive chlorophyll assessment in higher plant leaves," *J. Plant Physiol.*, vol. 160, no. 3, pp. 271–282, Mar. 2003.
- [30] S. Mishra and D. R. Mishra, "Normalized difference chlorophyll index: A novel model for remote estimation of chlorophyll-a concentration in turbid productive waters," *Remote Sens. Environ.*, vol. 117, pp. 394–406, Feb. 2012.
- [31] A. A. Gitelson and M. N. Merzlyak, "Remote sensing of chlorophyll concentration in higher plant leaves," *Adv. Sp. Res.*, vol. 22, no. 5, pp. 689–692, Jan. 1998.
- [32] C. S. T. Daughtry, C. L. Walthall, M. S. Kim, E. B. De Colstoun, and J. E. McMurtrey, "Estimating corn leaf chlorophyll concentration from leaf and canopy reflectance," *Remote Sens. Environ.*, vol. 74, no.



2, pp. 229–239, Nov. 2000.

- [33] G. Rondeaux, M. Steven, and F. Baret, “Optimization of soil-adjusted vegetation indices,” *Remote Sens. Environ.*, vol. 55, no. 2, pp. 95–107, Feb. 1996.
- [34] G. M. Smith and E. J. Milton, “The use of the empirical line method to calibrate remotely sensed data to reflectance,” *Int. J. Remote Sens.*, vol. 20, no. 13, pp. 2653–2662, Jan. 1999.
- [35] A. Stevens and L. Ramirez-Lopez, “An introduction to the prospectr package,” 2014.
- [36] L. Agisoft, “Agisoft Metashape Professional Edition.” Petersburg, 2019.
- [37] G. Bradski, “The openCV library,” *Dr. Dobb’s J. Softw. Tools*, 2000.
- [38] M. A. Fischler and R. C. Bolles, “Random Sample Consensus: A Paradigm for Model Fitting with Applications to Image Analysis and Automated Cartography,” in *Readings in Computer Vision*, Elsevier, 1987, pp. 726–740.

8 Appendix Image Data

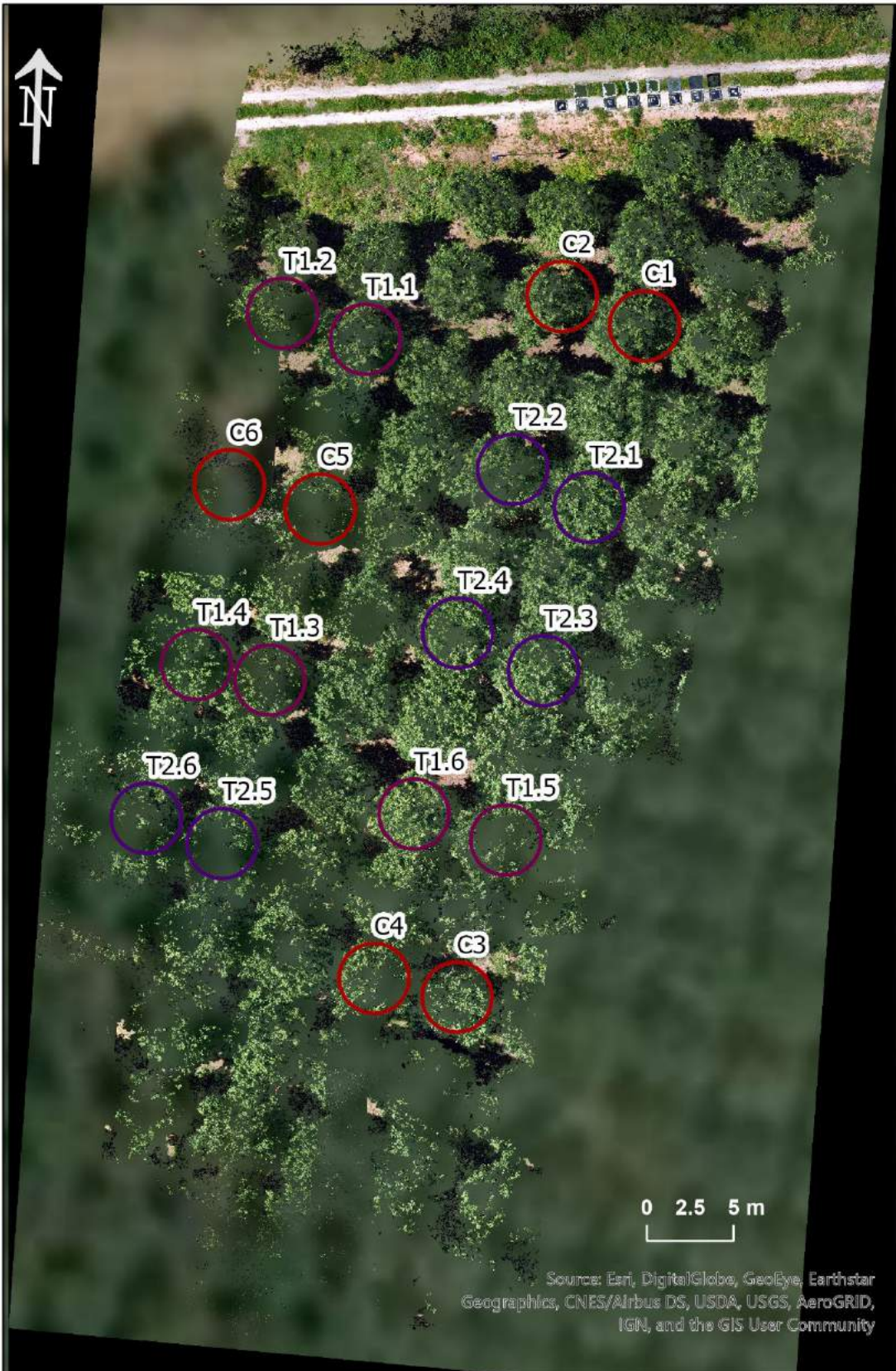


Figure A1: Sony orthomosaic 02/06/2019 (RGB), circled trees were surveyed during the pest and disease trial and represent T*: dates and C: control hazelnut trees



Figure A2: Sony orthomosaic 14/07/2019 (RGB)

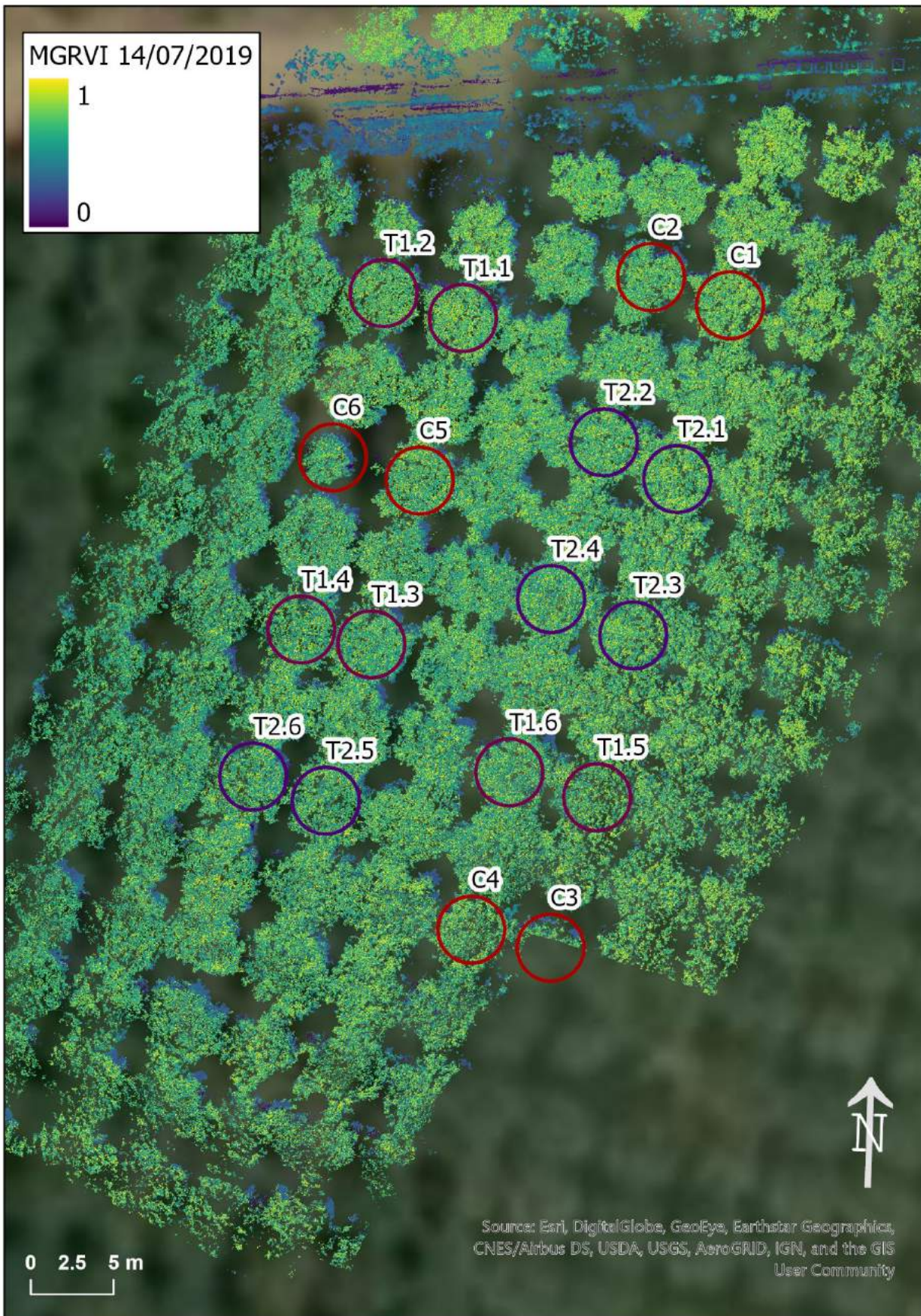


Figure A3: Sony orthomosaic MGRVI 14/07/2019

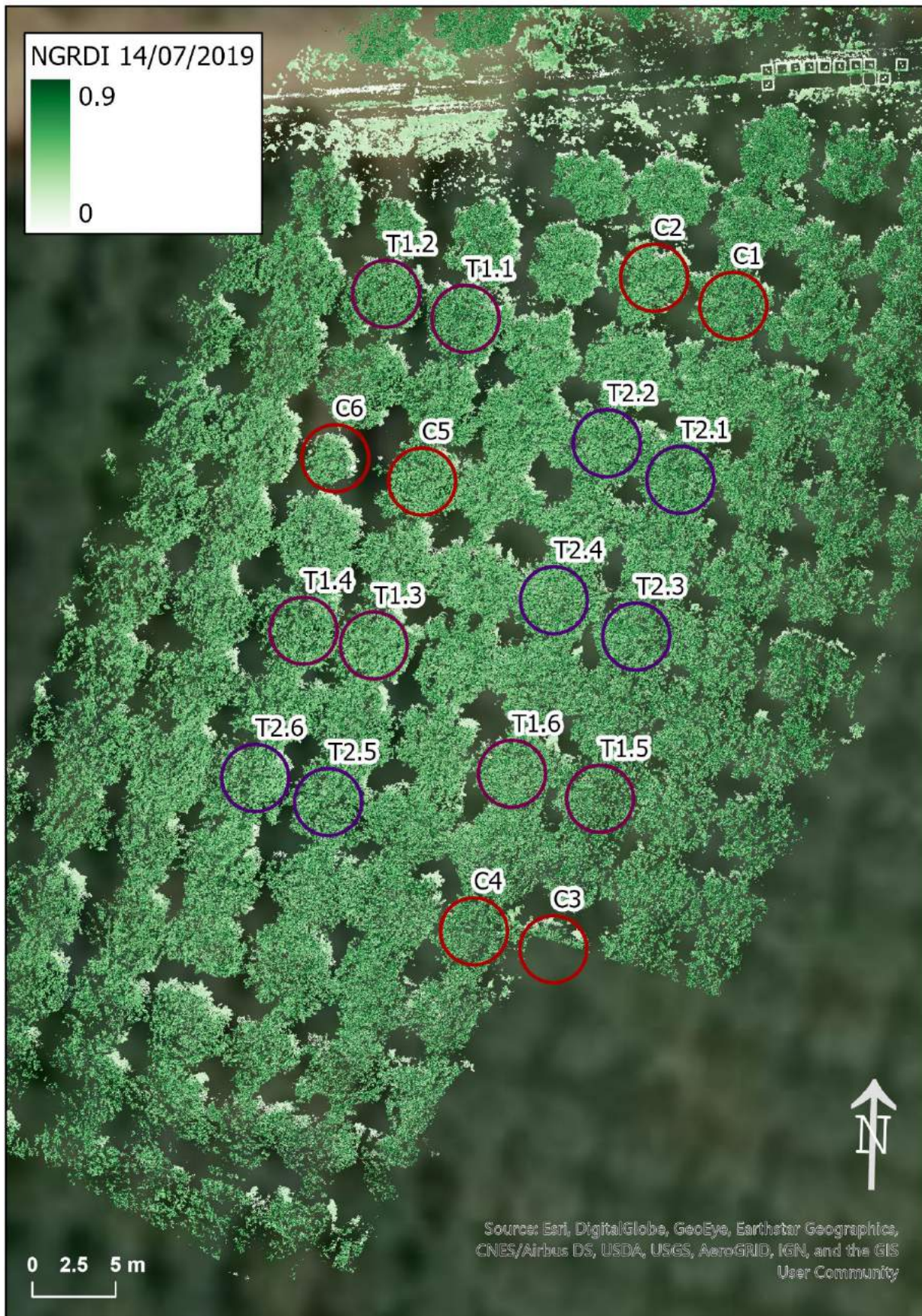


Figure A4: Sony orthomosaic NGRDI 14/07/2019

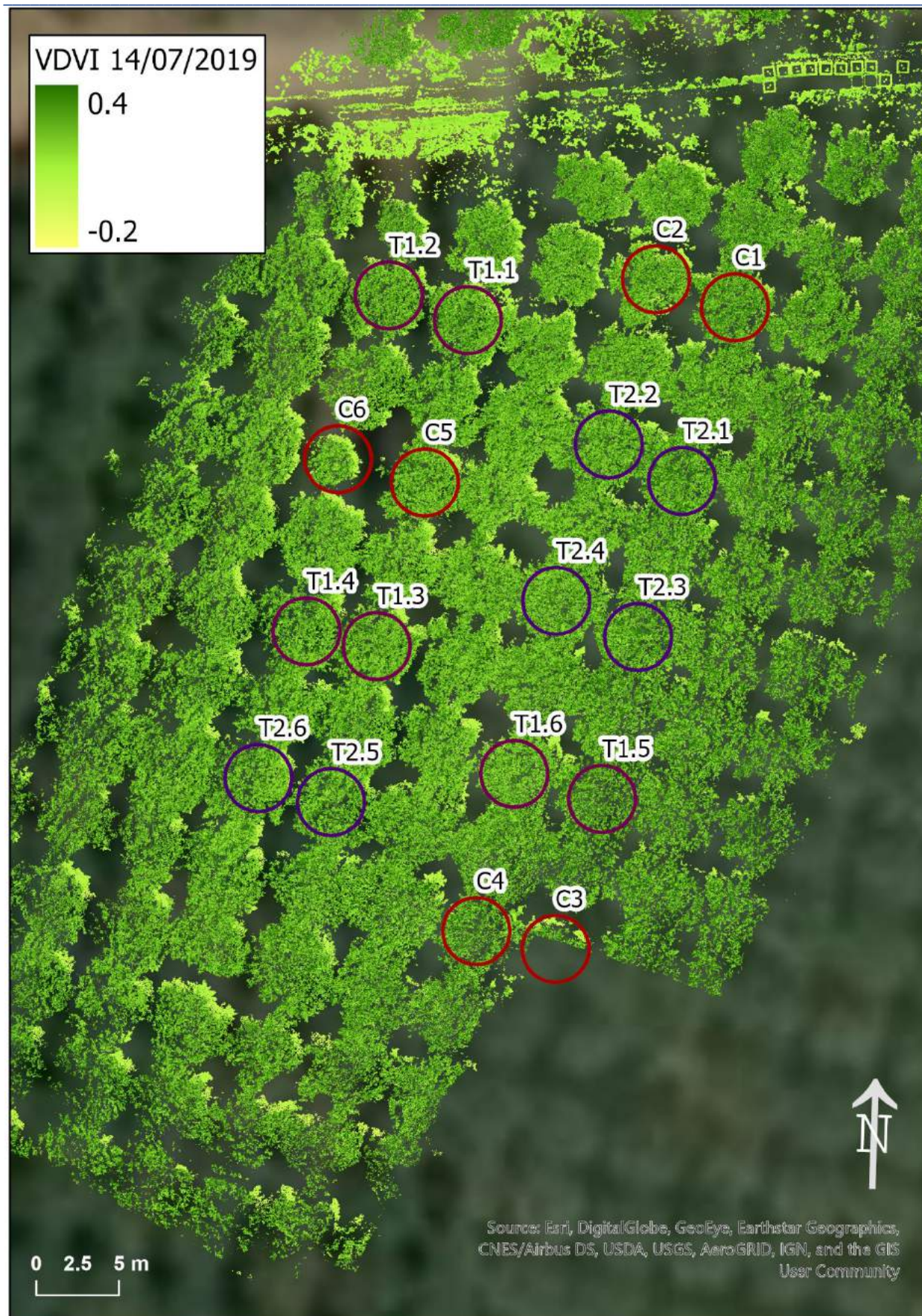


Figure A5: Sony orthomosaic VDMI 14/07/2019



Figure A6: Sony orthomosaic 21/07/2019 (RGB)

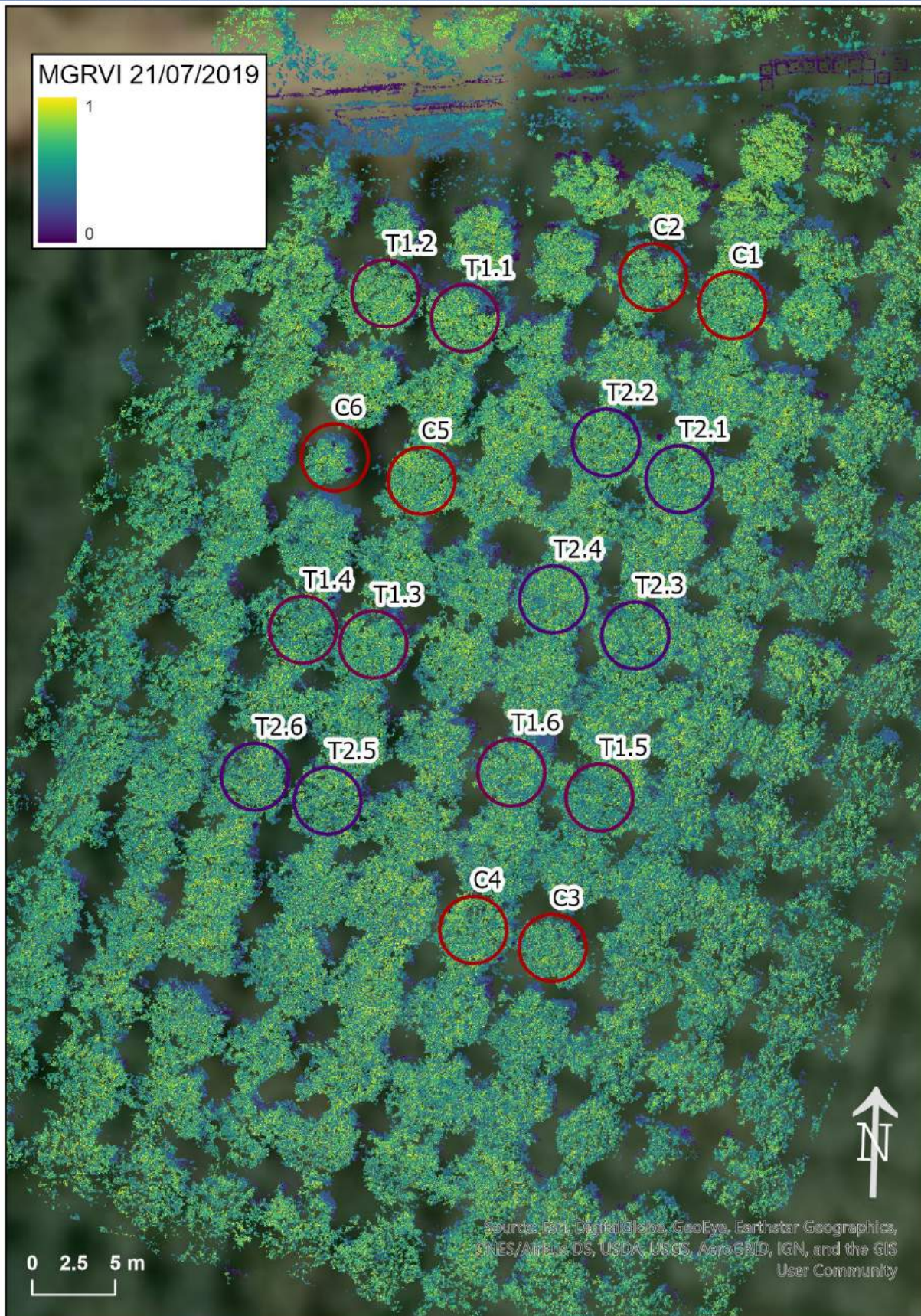


Figure A7: Sony orthomosaic MGRVI 21/07/2019

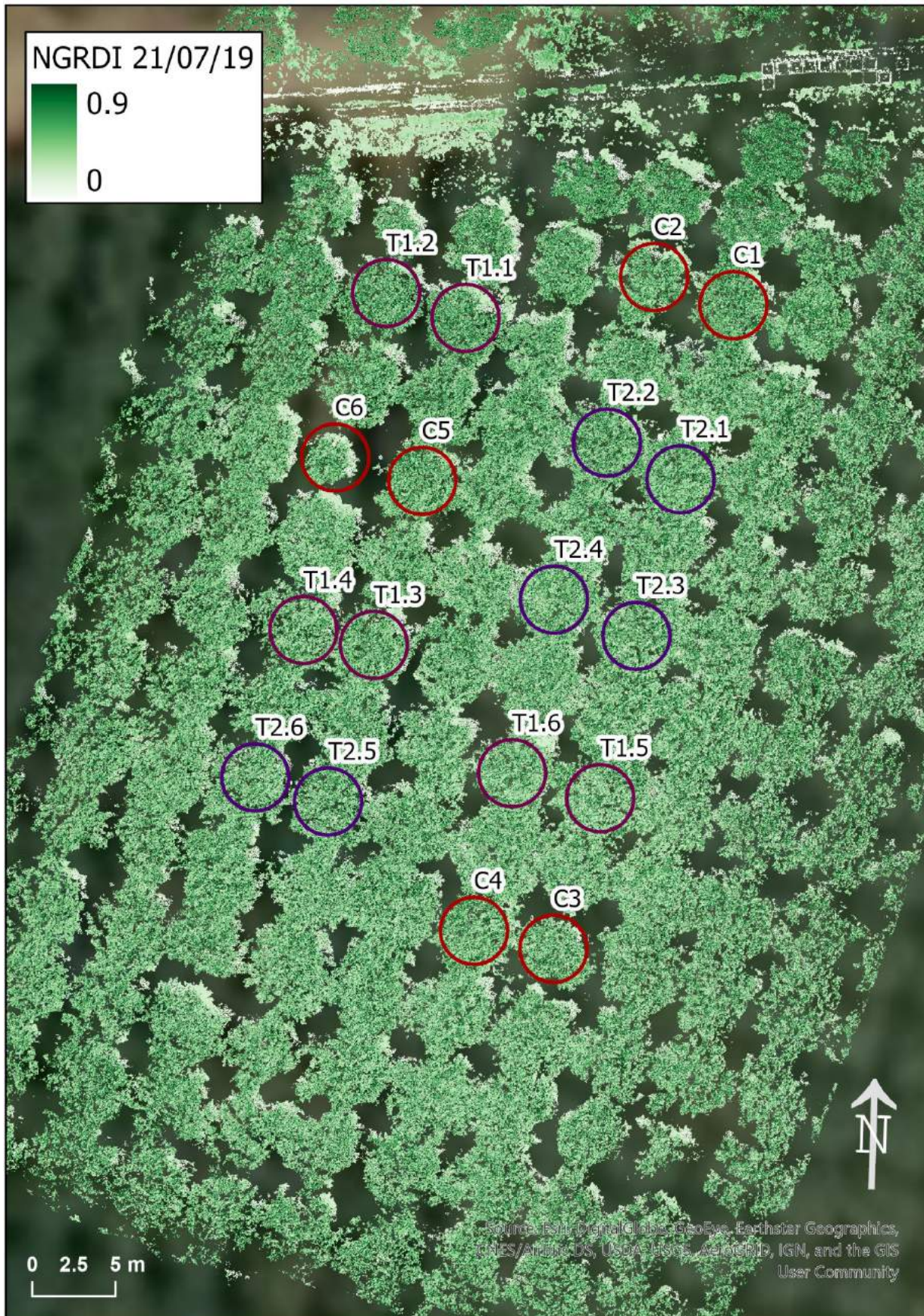


Figure A8: Sony orthomosaic NGRDI 21/07/2019

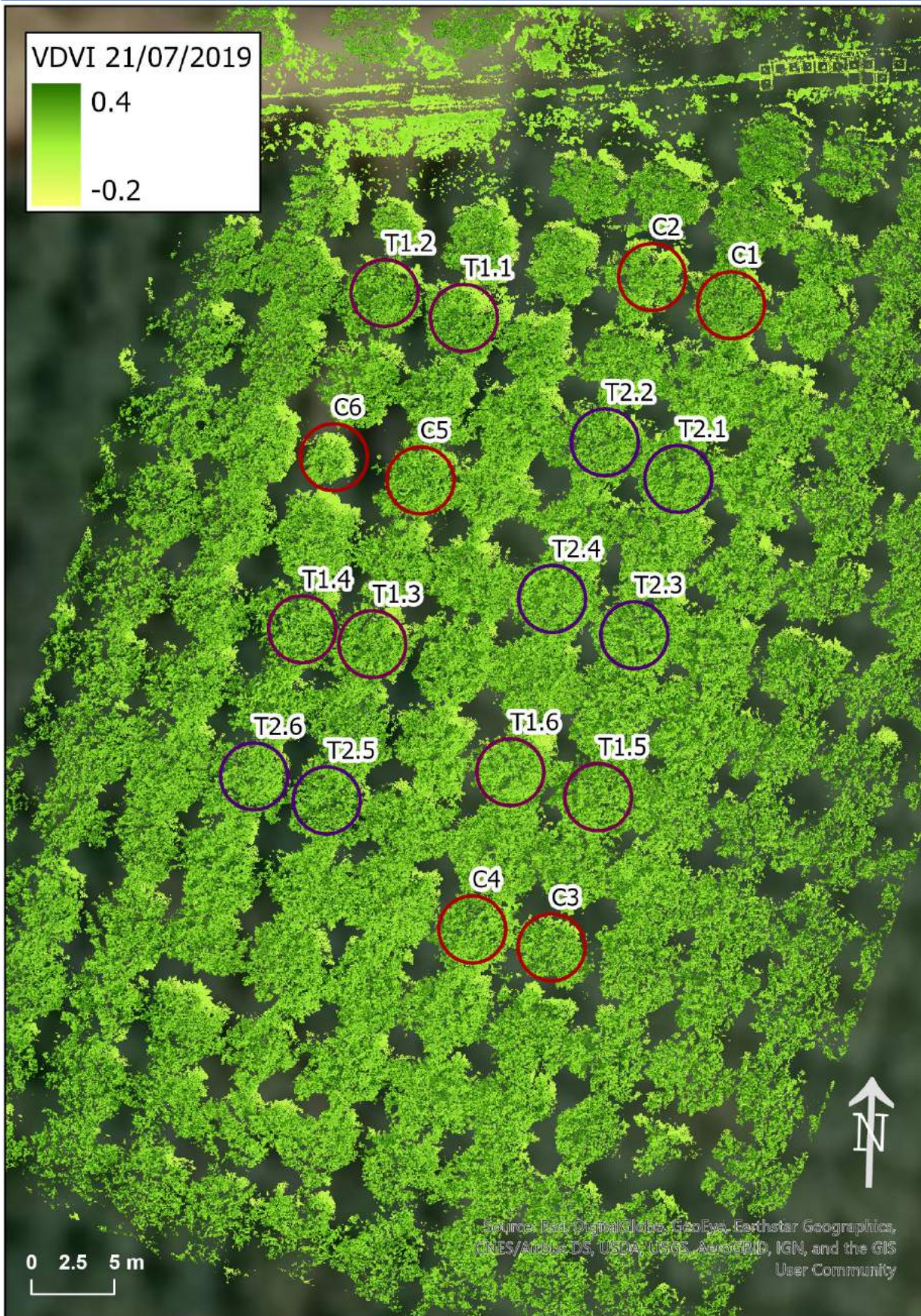


Figure A9: Sony orthomosaic VDV I 21/07/2019



Figure A10: Tetracam MCAW orthomosaic 21/07/2019 (R: 900nm, G: 680nm, B: 550nm)

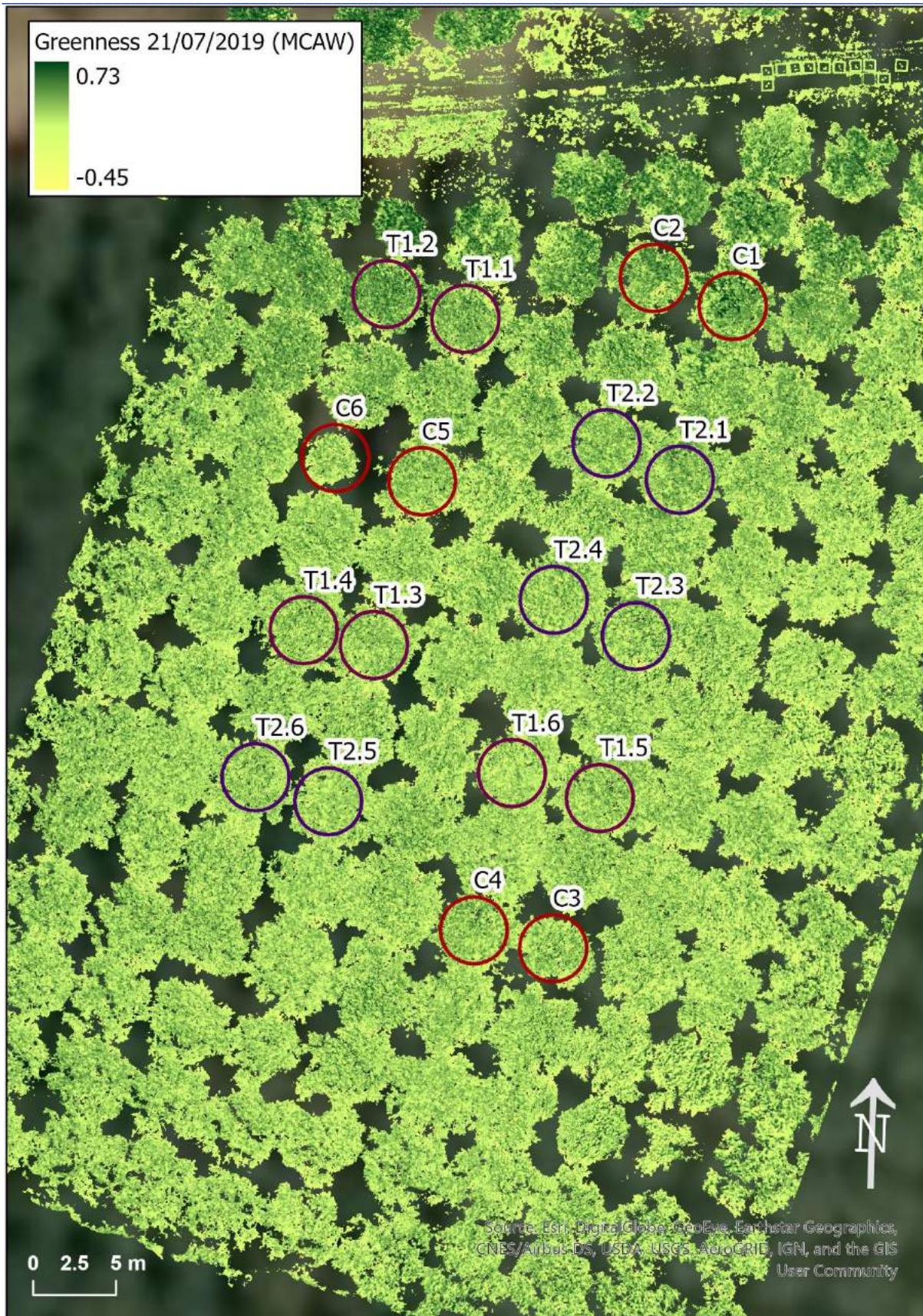


Figure A11: Tetracam MCAW orthomosaic Greenness Index 21/07/2019

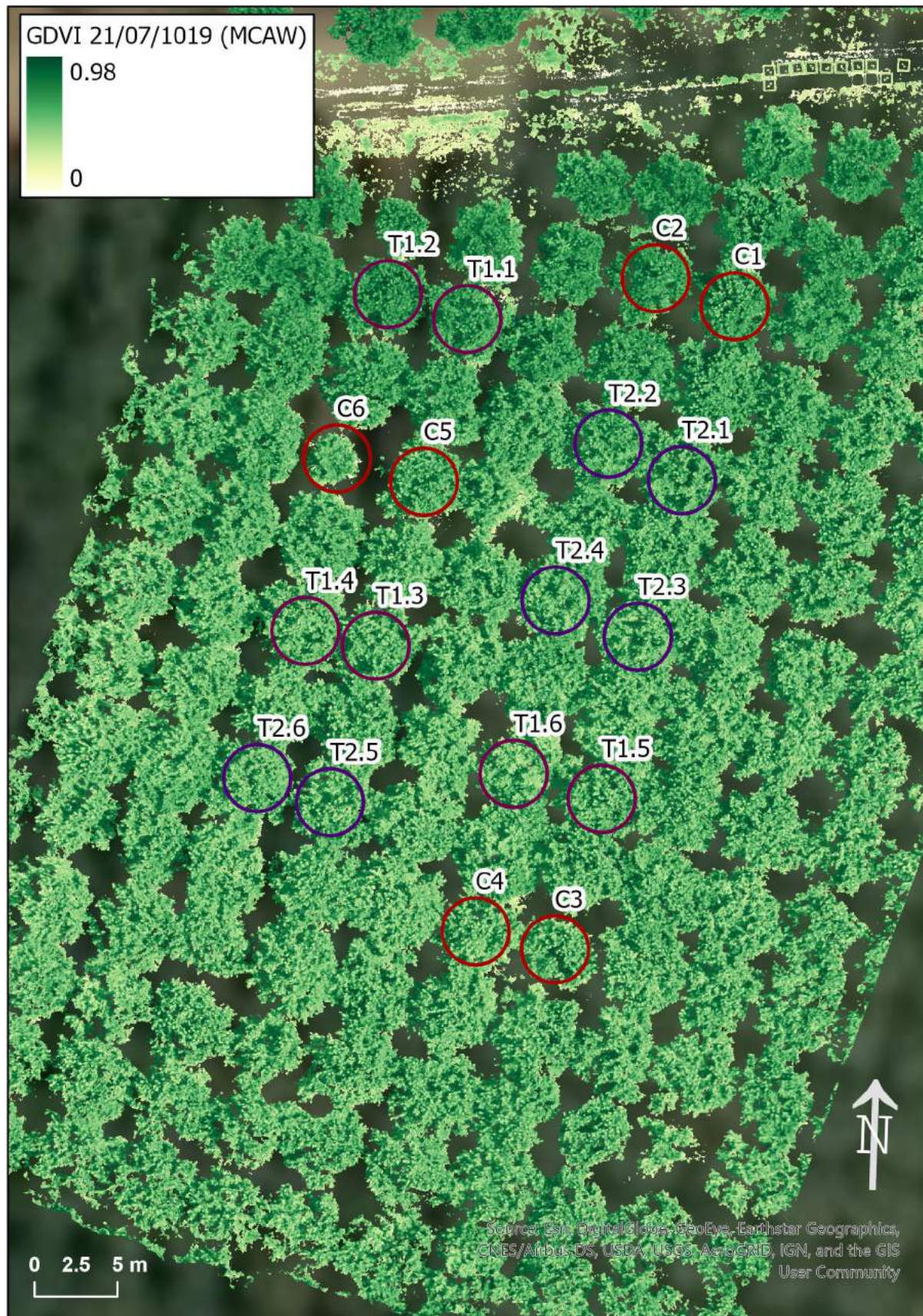


Figure A12: Tetracam MCAW orthomosaic GDVI 21/07/2019

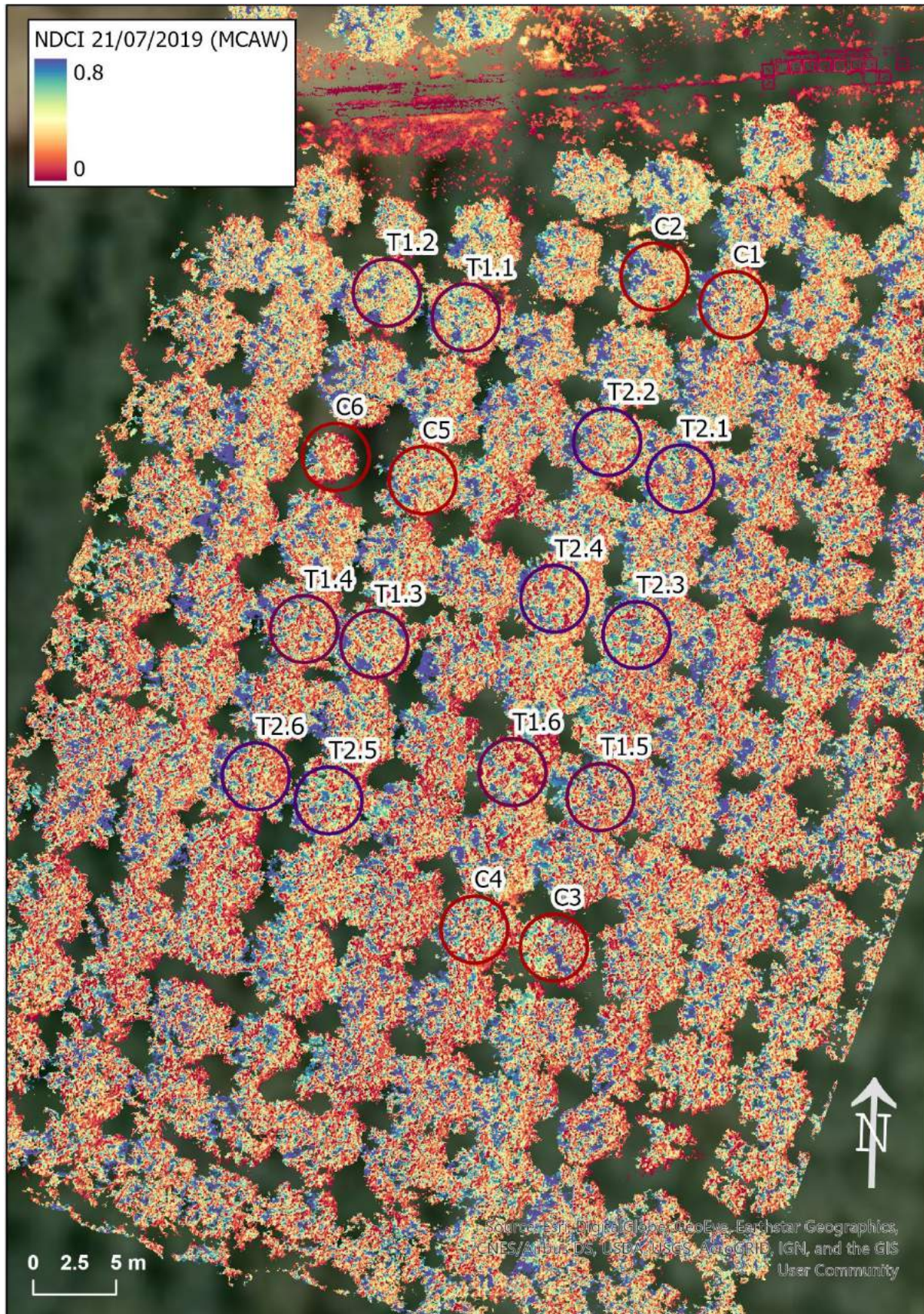


Figure A13: Tetracam MCAW orthomosaic NDCI 21/07/2019

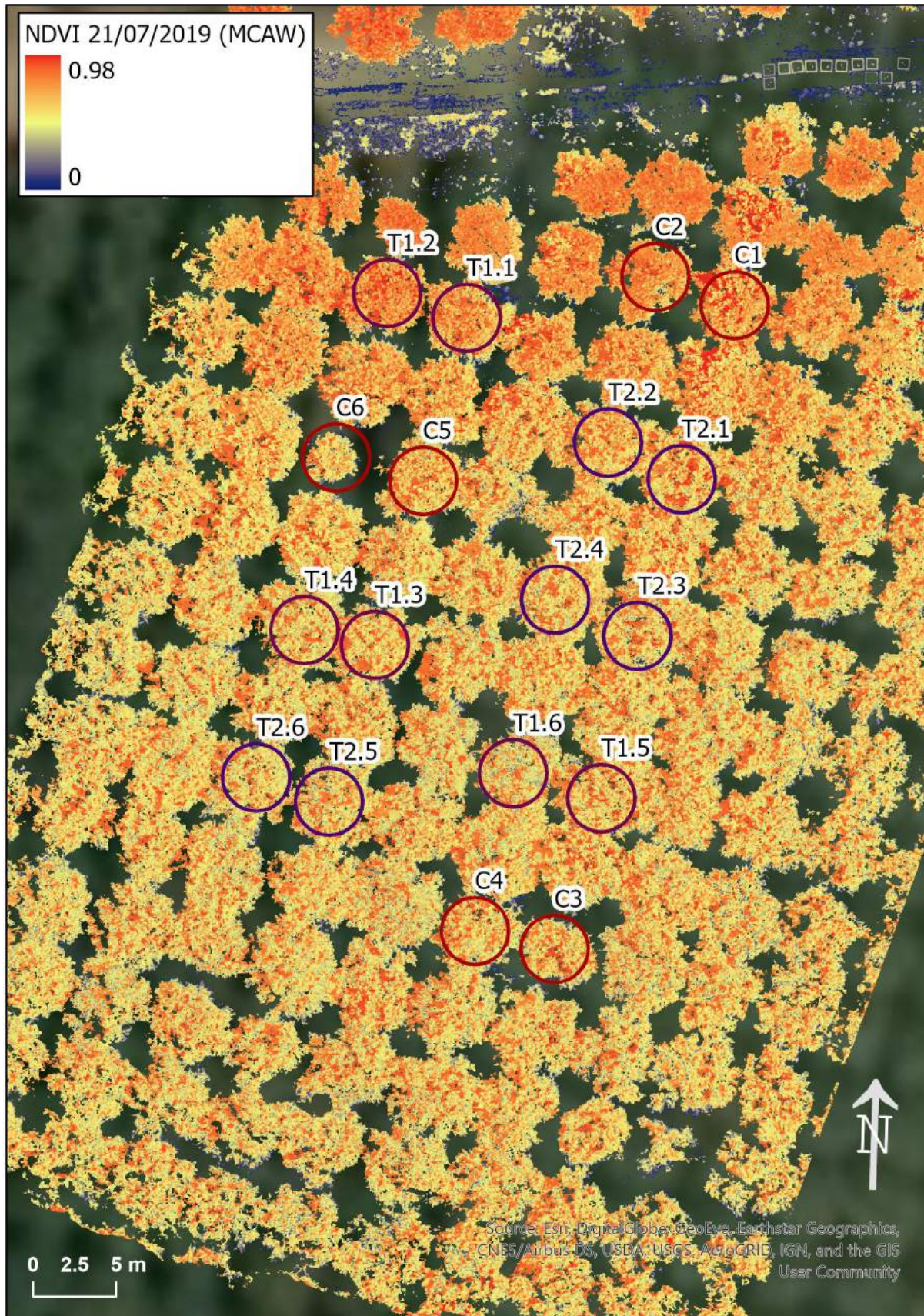


Figure A14: Tetracam MCAW orthomosaic NDVI 21/07/2019

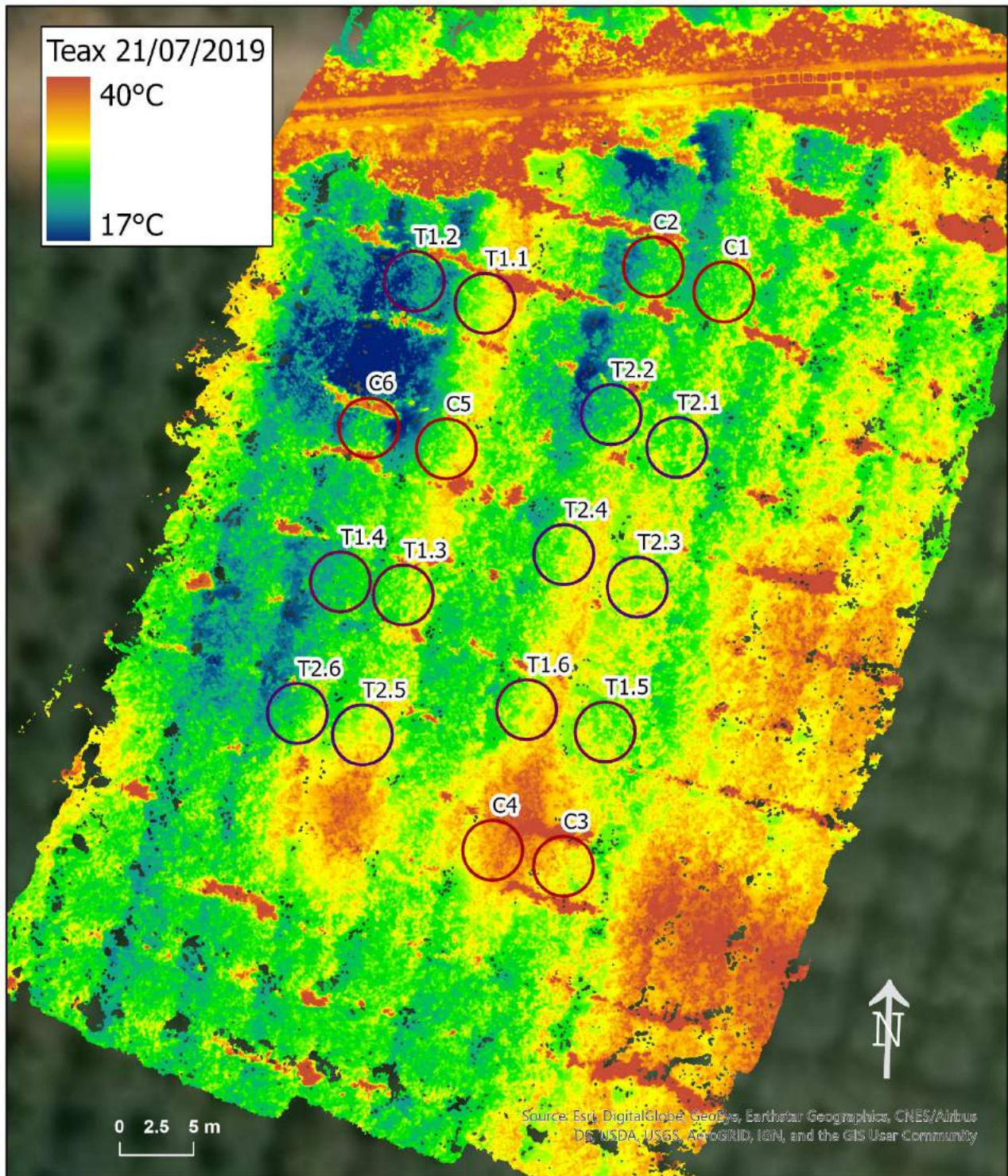


Figure A15: Thermal orthomosaic 21/07/2019

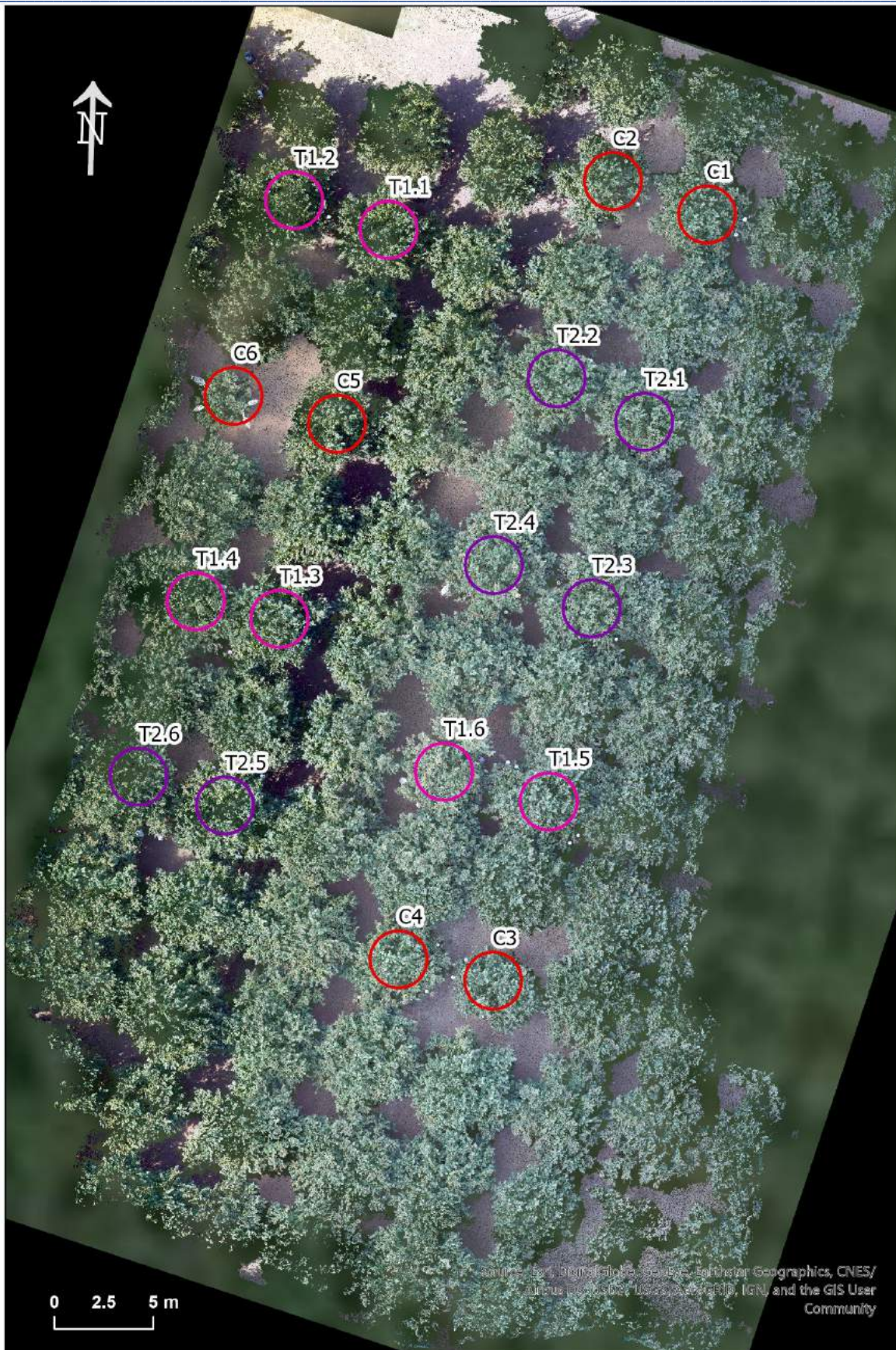


Figure A16: Sony orthomosaic 10/08/2019 (RGB)

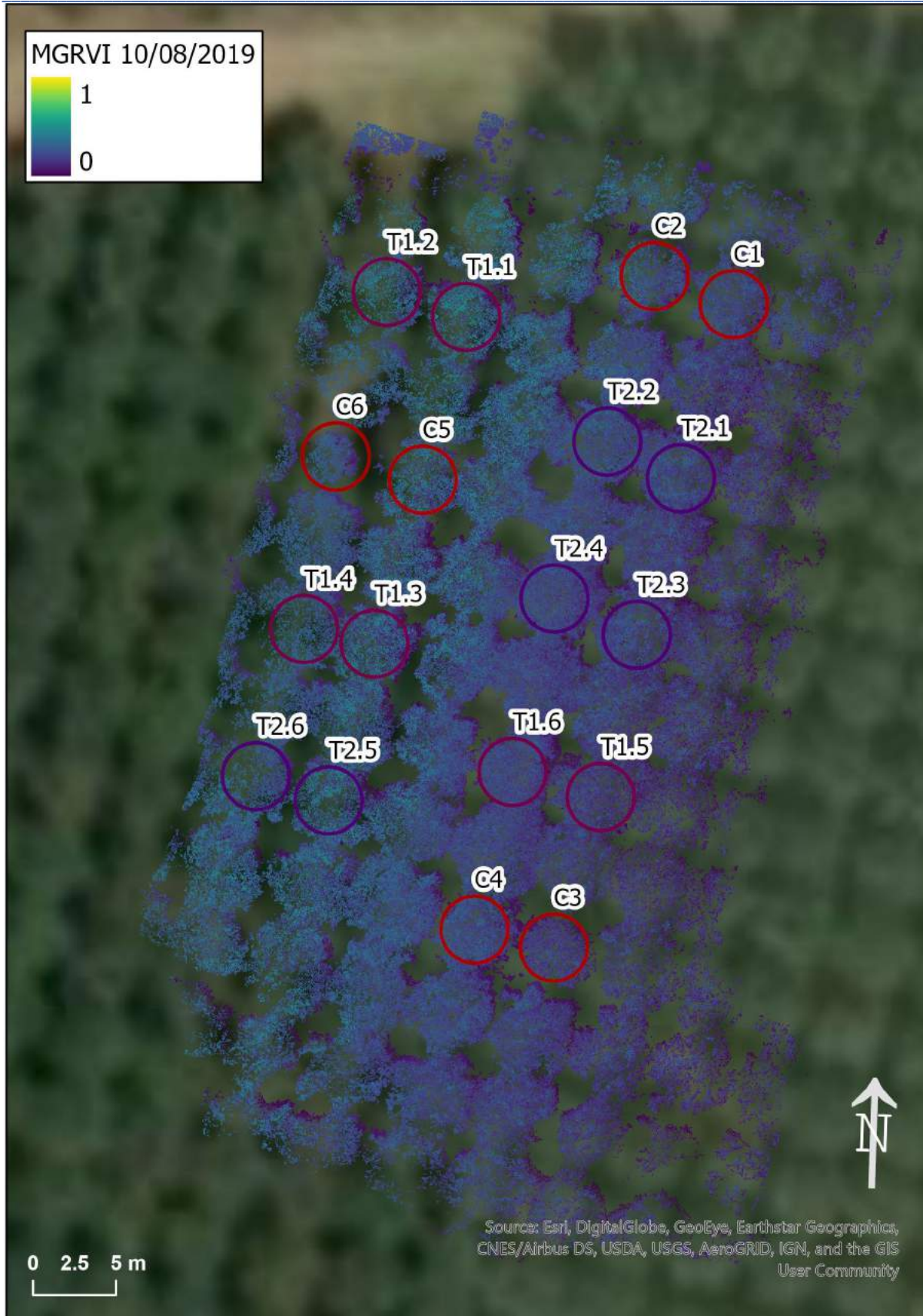


Figure A17: Sony orthomosaic MGRVI 10/08/2019

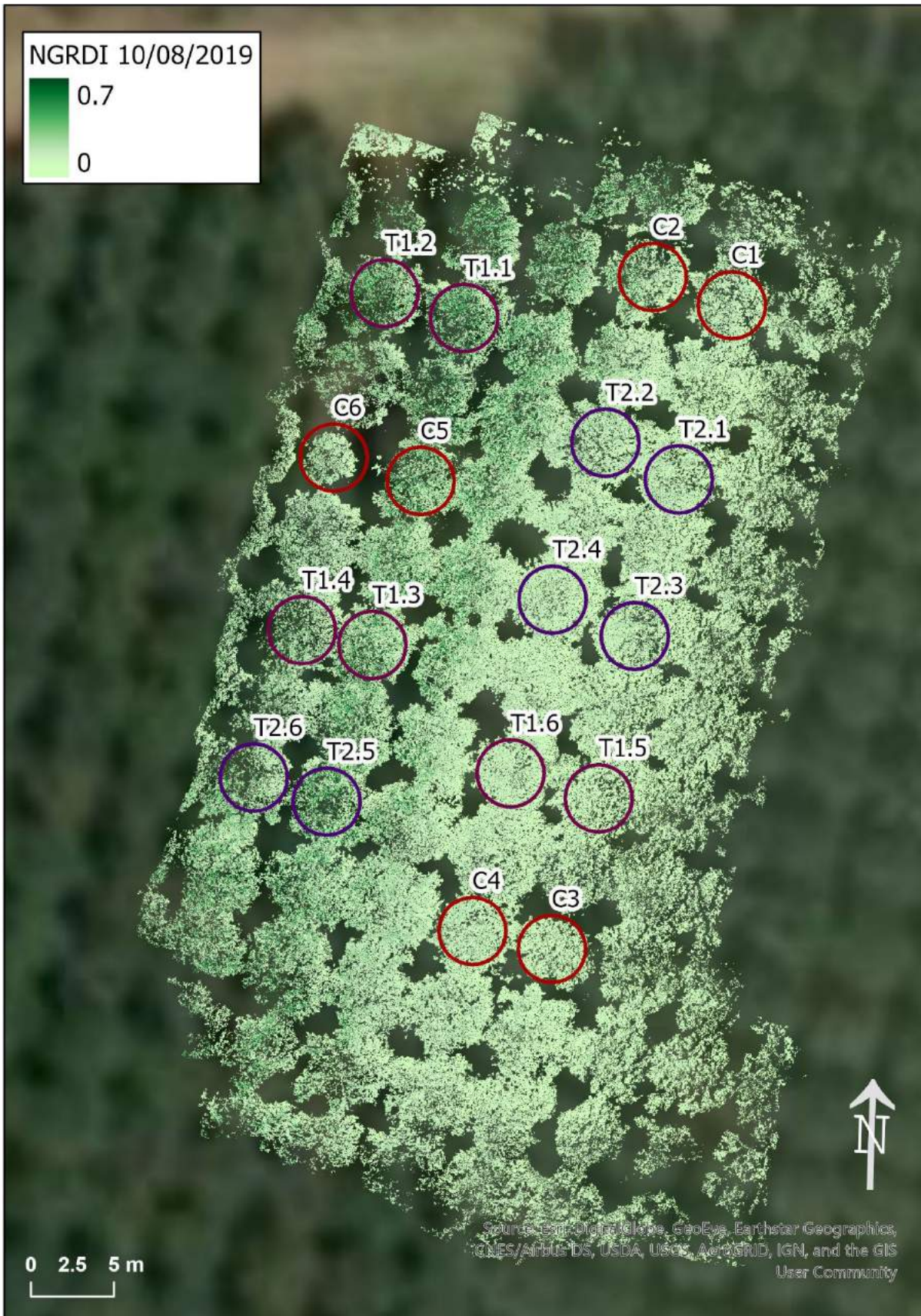


Figure A18: Sony orthomosaic NGRDI 10/08/2019

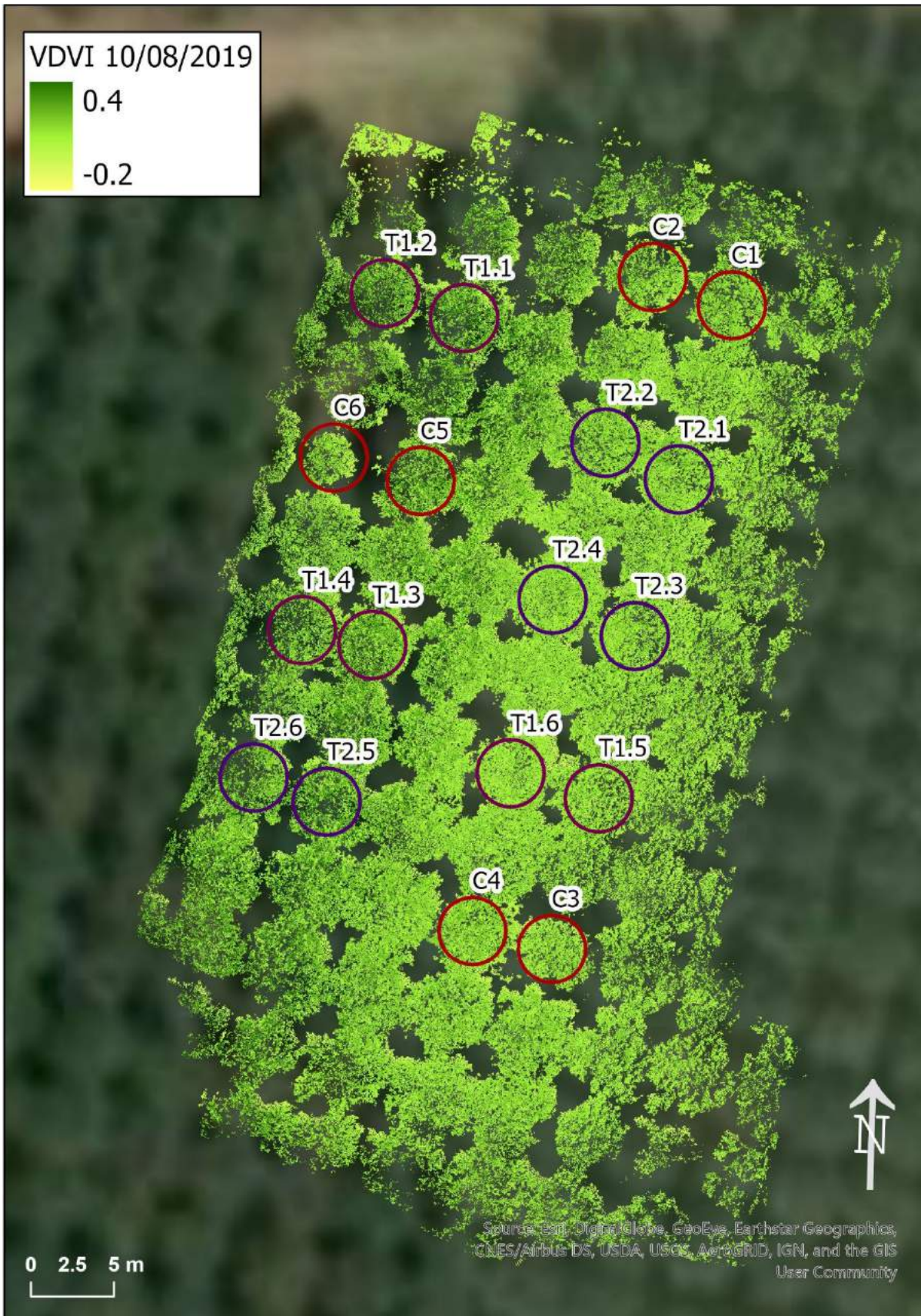


Figure A19: Sony orthomosaic VDMI 10/08/2019